



# AMERICAN METEOROLOGICAL SOCIETY

*Journal of Physical Oceanography*

## **EARLY ONLINE RELEASE**

This is a preliminary PDF of the author-produced manuscript that has been peer-reviewed and accepted for publication. Since it is being posted so soon after acceptance, it has not yet been copyedited, formatted, or processed by AMS Publications. This preliminary version of the manuscript may be downloaded, distributed, and cited, but please be aware that there will be visual differences and possibly some content differences between this version and the final published version.

The DOI for this manuscript is doi: 10.1175/JPO-D-16-0035.1

The final published version of this manuscript will replace the preliminary version at the above DOI once it is available.

If you would like to cite this EOR in a separate work, please use the following full citation:

Ezhova, E., C. Cenedese, and L. Brandt, 2016: Interaction between a vertical turbulent jet and a thermocline. *J. Phys. Oceanogr.* doi:10.1175/JPO-D-16-0035.1, in press.

© 2016 American Meteorological Society



# Interaction between a vertical turbulent jet and a thermocline

Ekaterina Ezhova\*

*Linné FLOW Centre and SeRC (Swedish e-Science Research Centre), KTH Mechanics,  
Stockholm, Sweden*

Claudia Cenedese

*Physical Oceanography Department, Woods Hole Oceanographic Institution, Woods Hole,  
Massachusetts*

Luca Brandt

*Linné FLOW Centre and SeRC (Swedish e-Science Research Centre), KTH Mechanics,  
Stockholm, Sweden*

\*Corresponding author address: Ekaterina Ezhova, Linné FLOW Centre and SeRC (Swedish e-Science Research Centre), KTH Mechanics, 10044 Stockholm, Sweden.

E-mail: ezhova@mech.kth.se

## ABSTRACT

14 We study the behaviour of an axisymmetric vertical turbulent jet in an un-  
15 confined stratified environment by means of well-resolved large eddy simu-  
16 lations. The stratification is two uniform layers separated by a thermocline.  
17 We consider two cases: when the thermocline thickness is small and of the  
18 order of the jet diameter at the thermocline entrance. The Froude number of  
19 the jet at the thermocline varies from 0.6 to 1.9 corresponding to the class  
20 of weak fountains. We quantify mean jet penetration, stratified turbulent en-  
21 trainment, jet oscillations and the generation of internal waves. The mean jet  
22 penetration is predicted well by a simple model based on the conservation of  
23 the source energy in the thermocline. The entrainment coefficient for the thin  
24 thermocline is consistent with the theoretical model for a two-layer stratifi-  
25 cation with a sharp interface, while for the thick thermocline entrainment is  
26 larger at low Froude numbers. We report the presence of a secondary horizon-  
27 tal flow in the upper part of the thick thermocline, resulting in the entrainment  
28 of fluid from the thermocline rather than from the upper stratification layer.  
29 The spectra of the jet oscillations in the thermocline display two peaks, at  
30 the same frequencies for both stratifications at fixed Froude number. For the  
31 thick thermocline, internal waves are generated only at the lower frequency,  
32 since the higher peak exceeds the maximal buoyancy frequency. For the thin  
33 thermocline, conversely, the spectra of the internal waves show the two peaks  
34 at low Froude numbers, whereas only one peak at the lower frequency is ob-  
35 served at higher Froude numbers.

## 36 **1. Introduction**

37 This study focuses on the dynamics of an axisymmetric vertical turbulent jet in a stratified fluid.  
38 Vertical turbulent jets may serve as models of numerous flows both in nature and industry (see  
39 e.g. Turner (1973); List (1982); Hunt (1994)) including effluents from submerged wastewater  
40 outfall systems in the ocean (e.g. Jirka and Lee (1994)), convective cloud flows in the atmosphere,  
41 pollutant discharge from industrial chimneys, subglacial discharge from glaciers (e.g. Straneo and  
42 Cenedese (2015)). The stratification considered is two layers of homogeneous fluids of different  
43 temperature separated by a relatively thin layer with a temperature jump - a thermocline. This  
44 configuration is a typical model of the upper thermocline layer in lakes, the pycnocline in the  
45 ocean, as well as thermal inversions in the atmosphere, when the sharp gradient of the scalar  
46 prevails significantly over the scalar change in the layers.

47 The dynamics of vertical jets is governed mainly by their volume, momentum and buoyancy  
48 fluxes, where the buoyancy of a jet is defined by the density difference between the jet and the  
49 surrounding medium, normalized by gravity. If the flow density is less than the density of the  
50 surrounding medium then the jet is positively buoyant, if heavier the jet is negatively buoyant,  
51 while it is neutrally buoyant if the densities are equal. In general, all the examples of turbulent jets  
52 in nature and industry mentioned above result from mixed sources of buoyancy and momentum (as  
53 a rule they are positively buoyant). However, jets effectively entrain the surrounding fluid, hence,  
54 when the source is located far enough from the pycnocline, the density of the flow at the pycnocline  
55 entrance is almost equal to the density of the lower layer of stratification. The dynamics of such a  
56 flow in the pycnocline can therefore be modelled employing a neutrally buoyant turbulent jet with  
57 positive vertical momentum in the lower stratification layer. In other words, an initially buoyant jet  
58 in the pycnocline can be modelled employing a neutrally buoyant jet provided they have the same

59 velocity and radius at the entrance of the pycnocline. The turbulent jet considered here results  
 60 from a momentum source of the same fluid as in the lower layer of stratification. When entering  
 61 the thermocline, it becomes a negatively buoyant jet, i.e. a fountain.

62 Stationary regimes of turbulent fountains have been extensively investigated in both homoge-  
 63 neous and linearly stratified media (Turner 1966; List 1982; Bloomfield and Kerr 1998, 2000;  
 64 Kaye and Hunt 2006; Burridge and Hunt 2012, 2013) revealing the dependency of the mean pen-  
 65 etration height and of the entrainment coefficient on the different parameters of the problem. The  
 66 behaviour of an axisymmetric miscible Boussinesq fountain in a homogeneous fluid is defined by  
 67 the Reynolds number  $Re = U_0 R_0 / \nu$  ( $U_0$  the inflow velocity,  $R_0$  the nozzle radius,  $\nu$  the fluid kine-  
 68 matic viscosity), and the Froude number  $Fr = U_0 / \sqrt{g' R_0}$  (with  $g' = g \Delta \rho / \rho_0$  the reduced gravity,  
 69  $\Delta \rho$  is the density difference between source and ambient fluid). The Reynolds number determines  
 70 whether the fountain is laminar or turbulent while the Froude number characterizes the ratio be-  
 71 tween momentum flux  $M_0$ , buoyancy flux  $F_0$  and volume flux  $Q_0$  of the fountain. Indeed, it can be  
 72 rewritten, following Kaye and Hunt (2006), as  $Fr \sim M_0^{5/4} / Q_0 F_0^{1/2}$ . The Froude number can also  
 73 be interpreted as the ratio between two length scales:  $l \sim M_0^{3/4} / F_0^{1/2}$ , known as the momentum  
 74 jet length (Turner 1966), and  $R_0 \sim Q_0 / M_0^{1/2}$  corresponding to the initial radius of the jet. Using  
 75 theoretical considerations and experimental validations, Kaye and Hunt (2006) classified foun-  
 76 tains according to their Froude number as: very weak ( $Fr \lesssim 1$ ), weak ( $1 \lesssim Fr \lesssim 3$ ) and forced  
 77 ( $Fr \gtrsim 3$ ). Later Burridge and Hunt (2012, 2013) extended the classification using more experi-  
 78 mental data, further dividing "weak fountains" into weak and intermediate, with a change from  
 79 weak to intermediate fountains at  $Fr \approx 1.7$ . The behaviour of forced fountains in a homogeneous  
 80 fluid is governed by the momentum and buoyancy fluxes and the mean penetration height, here  
 81 denoted  $h_z$ , is therefore proportional to the momentum jet length  $h_z / R_0 \sim Fr$  (Turner 1966). For  
 82 weak fountains, instead, all three fluxes are important and dimensional analysis gives a penetration

83  $h_z/R_0 \sim Fr^2$  (Kaye and Hunt 2006; Burrige and Hunt 2012). Finally, very weak fountains are  
84 hydraulically controlled and estimates at large Reynolds numbers give  $h_z/R_0 \sim Fr^{2/3}$  (Kaye and  
85 Hunt 2006; Burrige and Hunt 2012).

86 In a linear stratification dimensional considerations yield a penetration height  $h_z/R_0 \sim Fr^{1/2}$  for  
87 forced fountains with zero initial buoyancy flux (McDougall 1981; Bloomfield and Kerr 1998). In  
88 general, however, the rise height of a fountain in a stratified fluid depends on the density profile and  
89 requires more complicated numerical models based on the conservation laws for the momentum,  
90 volume and buoyancy fluxes of the jet (Morton et al. 1956; Bloomfield and Kerr 2000).

91 Instabilities are observed for fountains in a homogeneous fluid, and this oscillatory motion has  
92 become the object of research only recently (Friedman 2006; Friedman et al. 2007; Williamson  
93 et al. 2008; Burrige and Hunt 2013). The dynamics of a fountain in a homogeneous fluid is,  
94 analogously to the mean penetration height, fully controlled by the Froude and Reynolds num-  
95 bers. It has been demonstrated experimentally that weak fountains can undergo oscillations with  
96 amplitudes comparable to their heights and well-defined frequencies. The oscillatory dynamics of  
97 fountains in stratified fluids is however mostly unexplored. Interestingly, the only experimental  
98 investigation in a linear stratification has shown no direct connection between the frequency of the  
99 fountain oscillations and the frequency of internal waves (Ansong and Sutherland 2010).

100 A behavior similar to the oscillatory dynamics of weak fountains has been revealed in  
101 pycnocline-like stratified fluids while modelling submerged wastewater outfall systems in the  
102 ocean (Troitskaya et al. 2008). Turbulent buoyant plumes discharged horizontally into oceanic  
103 salt water gain vertical momentum due to their positive buoyancy while they propagate in the  
104 lower layer of stratification. At the same time they are mixing intensively with the surrounding  
105 fluid owing to the turbulent entrainment. At the entrance to the pycnocline, these jets have density  
106 close to the density of the lower layer of stratification and a non-zero vertical momentum thus

107 forming fountains. These fountains are capable to generate internal waves in a pycnocline through  
108 their oscillations. This effect has been demonstrated experimentally, by means of laboratory scale  
109 modeling of wastewater outfall systems, and later numerically (Druzhinin and Troitskaya 2012,  
110 2013) both for laminar and turbulent fountains/jets in two-layer stratified fluid with a thin pyc-  
111 nocline (i.e. in the presence of a rather sharp density jump compared to the jet diameter at the  
112 pycnocline entrance).

113 As mentioned earlier, fountains in a linear stratified fluid do not show pronounced oscillations,  
114 while fountains in a two-layers fluid are characterized by strong oscillations. Thus, in addition to  
115 the Reynolds and Froude number, with all these parameters taken in the vicinity of the pycnocline,  
116 the ratio of the pycnocline thickness to the jet diameter, is expected to play an important role.  
117 Therefore, the aim of this paper is to understand the influence of the ratio "pycnocline thickness/jet  
118 diameter" on the dynamics of a turbulent fountain and on the generation of internal waves, using  
119 data from well-resolved Large Eddy Simulation (LES). Since the pycnocline is subject to seasonal  
120 variability (Kamenkovich and Monin 1978; Knauss 2005; Stewart 2008) this ratio is expected to  
121 change throughout the year, making this a relevant question in oceanography.

122 Previous numerical investigations (Druzhinin and Troitskaya 2012, 2013) investigated a similar  
123 configuration but focused on a thin pycnocline in comparison to the jet diameter at the pycnocline  
124 entrance. However, field measurements and results of modelling employing nonhydrostatic gen-  
125 eral circulation model reveal that they are mostly of the same size (Sciascia et al. 2013; Troitskaya  
126 et al. 2008). In this paper we compare jet dynamics in two different stratifications: one with a  
127 thin thermocline, analogous to Druzhinin and Troitskaya (2013), and the other with a thermocline  
128 thickness close to the jet diameter at the thermocline entrance. The latter case, for the thermocline  
129 Froude numbers 0.87-1.16, reproduces the conditions of laboratory experiments investigating the  
130 generation of internal waves by a turbulent jet (Ezhova et al. 2012). Note, that the parameters of the

131 jet at the entrance to the thermocline in the experiments matched the parameters of the laboratory  
132 scale modelling of the real wastewater outfall system in winter conditions (Troitskaya et al. 2008).  
133 In summer, convection in the upper layer is weak, governed mainly by the surface wave breaking  
134 and mixing due to the wind, and together with the increased temperature difference between up-  
135 per and lower layers, this results in the sharpening of the pycnocline and its moving closer to the  
136 surface. As a result, for the same source location, the radius of the jet at the pycnocline entrance  
137 increases and the vertical velocity decreases; some qualitative conclusions about the jet dynamics  
138 in these conditions can therefore be drawn from the present results for the thin thermocline and  
139 low Froude numbers.

140 The jet dynamics in the thermocline is relevant for turbulent mixing of the jet with the surround-  
141 ing media. This important question has been before investigated for a jet in two-layers stratification  
142 with a density interface experimentally (Cotel et al. 1997; Lin and Linden 2005) and theoretically  
143 (Shrinivas and Hunt 2014, 2015). In this study we investigate the mean flows in the thermocline  
144 and compare the entrainment flux of the jet in stratifications characterized by a finite thickness of  
145 the thermocline with the results of the theoretical model by Shrinivas and Hunt (2014).

146 The paper is organized as follows. Section 2 contains the relevant equations and a brief descrip-  
147 tion of the LES model. The test case of a turbulent jet in a homogeneous medium is described and  
148 the setup of the simulations for a stratified case discussed. Section 3 is devoted to the results of the  
149 simulations: in the first part we investigate the penetration height and turbulent entrainment of the  
150 jet in a stratified medium and discuss the dynamics of the jet in the thermocline. The generation  
151 of the internal waves is presented in the second part. Our conclusions are given in Section 4.



## 152 2. Governing equations and numerical method

153 We consider a jet in an unconfined fluid with a stable thermal stratification. The dynamics of  
 154 a jet in a stratified fluid is governed by the Navier-Stokes equations for an incompressible fluid  
 155 with the Boussinesq approximation to model the buoyancy effects and a transport equation for the  
 156 temperature field. To carry out a parameter study like that presented here, we resort to LES to  
 157 reduce the computational costs. In a LES, the large turbulent eddies are fully resolved whereas the  
 158 effect of the smallest scales, those not resolved on the computational mesh, is modelled. A filter  
 159 is applied to derive an equation for the resolved scales that reads in dimensionless form and in a  
 160 Cartesian coordinate system

$$\frac{\partial u_i}{\partial t} + u_j \frac{\partial u_i}{\partial x_j} = -\frac{\partial p}{\partial x_i} + \frac{1}{Re} \frac{\partial^2 u_i}{\partial x_j^2} + \frac{1}{Fr^2} (T - T'_s) \delta_{iz} - \frac{1}{Re} \frac{\partial \tau_{ij}}{\partial x_j}, \quad (1)$$

$$\frac{\partial T}{\partial t} + u_j \frac{\partial T}{\partial x_j} = \frac{1}{RePr} \frac{\partial^2 T}{\partial x_j^2} - \frac{1}{Re} \frac{\partial \Theta_j}{\partial x_j} \quad (2)$$

$$\frac{\partial u_i}{\partial x_i} = 0. \quad (3)$$

161 The equations are made dimensionless with the initial jet diameter  $D_0$ , the jet maximal inflow  
 162 velocity  $U_0$ , and the temperature difference between the stratification layers  $\Delta T$ . We define the  
 163 profile of stratification as  $T'_s = (T_s - T_0)/\Delta T$ , where  $T_s$  is the undisturbed temperature profile and  
 164  $T_0$  is the temperature of the lower layer of stratification. The hydrostatic pressure component asso-  
 165 ciated with  $T'_s$  is subtracted from the full pressure to get  $p$  in our system. We define the Reynolds  
 166 number  $Re = \frac{U_0 D_0}{\nu}$ , the Froude number  $Fr = \frac{U_0}{\sqrt{g' D_0}}$ , with  $g' = \frac{g \Delta \rho}{\rho_0} \approx g a_T \Delta T$  the reduced grav-  
 167 ity (here  $a_T$  is the thermal expansion coefficient), the Prandtl number  $Pr = \frac{\nu}{\kappa}$  where  $\nu$  is the fluid  
 168 kinematic viscosity and  $\kappa$  the thermal conductivity.  $\tau_{ij}$  and  $\Theta_j$  are the fluxes representing the  
 169 subgrid Reynolds stresses and turbulent heat transport.

170 To model the subgrid-scale stresses we employ the dynamic Smagorinsky model (Smagorinsky  
 171 1963; Germano et al. 1991) which has been successfully used in the simulations of buoyant flows  
 172 by several authors, e.g. Pham et al. (2006, 2007). The subgrid-scale stresses are expressed as

$$\tau_{ij} = -2\nu_t S_{ij}, \quad S_{ij} = \frac{1}{2} \left( \frac{\partial u_i}{\partial x_j} + \frac{\partial u_j}{\partial x_i} \right), \quad (4)$$

$$\Theta_j = -\frac{\nu_t}{Pr_t} \frac{\partial T}{\partial x_j}. \quad (5)$$

173 In the spirit of the Prandtl mixing length model, the subgrid-scale viscosity is given by the formula

$$\nu_t = (C_s \Delta)^2 |S_{ij}|, \quad (6)$$

174 where  $\Delta = (\Delta x \Delta y \Delta z)^{1/3}$  and  $C_s$  is the Smagorinsky coefficient, related to the dynamic Smagorinsky  
 175 constant by  $C_s = \sqrt{C_d}$ . The idea underlying the dynamic Smagorinsky model is that the small  
 176 eddies of the large structures that are still resolved in the computations are statistically analogous  
 177 to the subgrid-scale eddies. Thus an additional filter, the test filter, is used to separate the resolved  
 178 turbulent spectrum and calculate dynamically the Smagorinsky constant  $C_d$  (for more detail see  
 179 Germano et al. (1991)).

180 In our simulations, the jet is generated by a round source of diameter  $D_0$  with an initial vertical  
 181 velocity profile

$$U_i = -0.5 \tanh \frac{r - 0.4}{0.05} + 0.5, \quad (7)$$

182 where  $r = \sqrt{x^2 + y^2}$ , with  $x$  and  $y$  the horizontal directions, see Fig. 1. The stratification of the  
 183 ambient fluid is of a thermocline-type with a temperature jump at the vertical position  $z = z_p$ . The  
 184 stratification profile is given by

$$T'_s = \frac{1}{2} (1 + \tanh(\gamma(z - z_p))) \quad (8)$$

185 where  $\gamma = D_0/H$  and  $H$  is the half-thickness of the thermocline. The temperature of the fluid at  
 186 the inflow is equal to the temperature of the lower stratification layer.

187 *a. Numerical method*

188 The numerical simulations presented here are performed with the parallel flow solver Nek5000  
189 (Fischer et al. 2008). The dynamic Smagorinsky model is built-in inside this code. Nek5000 is a  
190 spectral element code with exponential accuracy within the spectral elements. On each element  
191 the flow variables are represented as a superposition of Lagrange polynomials based on Gauss-  
192 Lobatto-Legendre quadrature points (GLL points). In the present calculations the spatial dis-  
193 cretization is made with polynomials of order 7, which means that each element contains  $8 \times 8 \times 8$   
194 grid points or GLL points. Time discretization involves an operator-splitting method using back-  
195 ward differentiation of order 2 for the implicitly treated viscous terms and 2nd order extrapolation  
196 for the explicitly treated convective terms (BDF2/EXT2). For stabilization, the highest 2 modes of  
197 each element are slightly dampened (5%). The test filter required for the calculations in the frame-  
198 work of the dynamic Smagorinsky model affects the 3 highest polynomial modes with a cut-off of  
199 0.05, 0.5 and 0.95 (Ohlsson et al. 2010).

200 Among the advantages of the spectral element method is the flexibility to construct spatially  
201 inhomogeneous meshes. For the particular problem at hand, one needs to resolve the small scales  
202 at the jet inflow to accurately reproduce the region of high kinetic energy production and the small  
203 scales in the region where the jet impinges on the pycnocline, producing high shears. At the same  
204 time, internal gravity waves are characterized by long wavelengths, large-scale motions, so that a  
205 lower resolution is enough at larger distances from the jet axis.

206 *b. Validation for the turbulent jet in a non-stratified fluid*

207 To validate the current implementation and be sure to have a fully developed turbulent jet at  
208 the thermocline entrance, we perform LES of a turbulent jet in a homogeneous fluid and compare

209 the main flow statistics with the data available in literature, both from experiments and Direct  
 210 Numerical Simulations (DNS).

211 The governing equations for a turbulent jet in a homogeneous fluid reduce, after the LES-  
 212 filtering, to

$$\frac{\partial u_i}{\partial t} + u_j \frac{\partial u_i}{\partial x_j} = -\frac{\partial p}{\partial x_i} + \frac{1}{Re} \frac{\partial^2 u_i}{\partial x_j^2} - \frac{1}{Re} \frac{\partial \tau_{ij}}{\partial x_j}, \quad (9)$$

$$\frac{\partial u_i}{\partial x_i} = 0. \quad (10)$$

213 The jet is generated at the bottom boundary of the computational domain and has a round shape  
 214 of diameter  $D_0$  with the initial velocity profile given in eq. (7). To trigger transition to turbulence,  
 215 we add to this laminar profile a set of 10 sinusoidal disturbances with frequencies  $f$  distributed  
 216 evenly in the range  $[0.05:5]$ , wavelengths in  $x, y$  directions changing from 4 minimal distances  
 217 between GLL points ( $\Delta x = \Delta y = 0.03$ ) to 20 these distances and random phases. The amplitude  
 218 of the disturbances is about 15% of the base flow velocity at the inflow. The simulations are  
 219 performed for Reynolds number  $Re = 15000$ .

220 We solve the governing equations on a rectangular domain of dimensions  $40 \times 40$  along the hor-  
 221 izontal  $x$  and  $y$ -axes, and 42 in the vertical direction (Fig. 1). We impose a traction free boundary  
 222 condition (open boundaries) at the lateral boundaries and the convective boundary condition by  
 223 Orlansky (1976)

$$\frac{\partial u_i}{\partial t} + c_{zi} \frac{\partial u_i}{\partial z} = 0 \quad (11)$$

224 at the top of the domain. Here  $c_{zi}$  are the components of the phase velocity that are calculated  
 225 dynamically for each velocity component at the  $z$ -level adjacent to the upper boundary and filtered  
 226 over the  $xy$ -plane by a running average. Negative values of  $c_{zi}$  are set to 0.

227 The mesh used is constructed following the guidelines in Picano and Hanjalic (2012): in the  
228 region closest to the jet inflow,  $x, y \in [-1.5, 1.5]$ ,  $z \in [0, 12]$ , a better resolution is achieved with  
229 uniform spectral elements of size  $\Delta x = \Delta y = 0.5$  and  $\Delta z = 0.6$  (each element containing  $8 \times 8 \times$   
230  $8$  GLL points). From the boundaries of this inner region, we stretch the grid by a factor 1.17  
231 along the horizontal axes and 1.06 along the  $z$ -axis. The total number of elements used in these  
232 validation runs is  $30 \times 30 \times 30$  corresponding to  $\approx 9$  million grid points. The timestep chosen for  
233 the calculation is 0.01, which amounts to keeping the CFL number below 0.25-0.3.

234 The values of  $C_d$  in the model are averaged over the vertical direction in a conical region con-  
235 taining the jet, resulting in a value of the Smagorinsky coefficient  $C_s$  in the range between 0 and  
236 0.2, in agreement, for example, with the values obtained in the simulations of buoyant plumes by  
237 Pham et al. (2007). The calculations of the statistics start approximately 100 time units after the  
238 jet has reached the upper boundary and extend over a time interval of over 500 dimensionless time  
239 units corresponding to  $\approx 30$  eddy turnover times if the characteristic velocity and the jet diameter  
240 are taken at  $z = 18$ .

241 Fig. 2a displays the inverse centerline mean velocity  $U_c$  versus the vertical coordinate  $z$  to show  
242 that the velocity follows the  $1/z$  dependence that can be derived from the momentum integral for  
243 a submerged turbulent jet. The asymptotic behavior starts from  $z \approx 12$ . The linear fit yields a  
244 slope of 0.22, corresponding to 0.165 if recalculated for the initial top-hat velocity profile with the  
245 same momentum and volume fluxes. This is in good agreement with the widely assumed values  
246 of 0.16-0.17 (see, for instance, Pope (2000)).

247 Fig. 2b displays the average  $z$ -velocity profile in the far-field of the jet in self-similar coordinates  
248 ( $\xi \sim r/(z - z_0)$ ,  $U/U_c$ ), where  $z_0$  denotes the location of the jet virtual origin and  $U_c$  corresponds  
249 to the maximum velocity at each  $z$ -level. In practice, we first compute the profiles at each  $z$  in self-  
250 similar variables and then average over the different profiles in the range  $z \in [14, 35]$ , following

251 Picano and Hanjalic (2012) among others. In the figure, we include for comparison the data from 2  
252 sets of DNS for the round and annular jets (Picano and Hanjalic 2012; Picano and Casciola 2007)  
253 and 2 laboratory experiments (Panchapakesan and Lumley 1993; Hussein et al. 1994) to confirm  
254 the accuracy of the results.

255 Figs. 2c and d report the turbulent stresses  $\langle u_z'^2 \rangle / U_c^2$  and  $\langle u_r'^2 \rangle / U_c^2$  in the far-field of the  
256 turbulent jet together with the data from the experiments and DNS mentioned above. To obtain  
257  $\langle u_r'^2 \rangle$  in the rectangular geometry, we measure the profiles of  $\langle u_x'^2 \rangle$  along the  $x$ -axis and of  
258  $\langle u_y'^2 \rangle$  along the  $y$ -axis and then average over the positive and negative  $x$  and  $y$  directions. We  
259 scale the profiles using the self-similar coordinates and average among the different  $z$  locations as  
260 described before. It can be seen in the figure that the agreement between the different set of data  
261 is good. Given these data, we consider a developed turbulent jet from  $z=14$  and therefore set, in  
262 the calculations in a stratified medium, the thermocline lower boundary at  $z = 20$ .

### 263 *c. Configuration of the jet in a stratified fluid*

264 Using the governing equations for a flow in a stratified medium in (1)-(3), we perform 2 series  
265 of simulations with the stratification profile in eq. (8). The first set assumes  $\gamma = 2$  and  $z_p = 20.5$   
266 which corresponds to a relatively thin thermocline since the jet diameter at the entrance to the  
267 thermocline, is approximately 4-5, as shown by the simulation of a turbulent jet in homogeneous  
268 medium presented in the previous section. Indeed, for  $\gamma = 2$  the thermocline is 4-5 times thinner  
269 than the diameter of the jet. The second set of simulations assumes  $\gamma = 0.5$  and  $z_p = 22$ , which we  
270 will denote as the thick thermocline; in this case, the thermocline thickness is approximately the  
271 same as the jet diameter at the thermocline entrance. In both series we perform calculations for 5  
272 different Froude numbers ( $Fr = 7, 10, 13, 16, 22$ ).

273 A better definitions of the Froude number and  $\gamma$  may consider values at the entrance to the  
 274 thermocline which is defined from the simulations at approximately  $z = 18$  (as it will be seen from  
 275 what follows), corresponding to  $Fr_t = 0.6, 0.86, 1.11, 1.37, 1.89$  (here  $Fr_t = u_t / \sqrt{g'R_t}$  where  $u_t$   
 276 and  $R_t$  are the mean jet velocity and radius as defined by Shrinivas and Hunt (2014)). We define  
 277 the ratio of the jet radius at the thermocline to the thermocline thickness,  $\gamma_t = R_t/H$ . For the thick  
 278 thermocline  $\gamma_t = 1$ , while for the thin thermocline  $\gamma_t = 4$ .

279 The choice of  $Fr_t \sim 1$  is justified by the observations by Burrige and Hunt (2013) of the sudden  
 280 jump in the amplitude and frequency of the fountain top oscillations in a homogeneous fluid.  
 281 Note however that the Reynolds number in the experiments of Burrige and Hunt (2013),  $Re \approx$   
 282  $1000 - 3500$ , is significantly lower than in our simulations. The experimental investigation of  
 283 turbulent jets in a stratified fluid by Ezhova et al. (2012) corresponds to  $Fr_t \sim 1$  and  $Re \sim 10000$ .  
 284 Given that the diameter of the jet in the experiments was comparable to the thermocline width, we  
 285 in fact reproduce these experimental conditions in the setup with the thick thermocline.

286 The coefficient of the dynamic Smagorinsky model,  $C_d$ , is averaged over the vertical direction  
 287 from  $z = 0$  to the maximum fountain penetration point for  $r < 5$  and from  $z = 17$  to the upper  
 288 boundary of the thermocline for  $r > 5$ , resulting in the same range of the Smagorinsky coefficient  
 289  $0 < C_s = \sqrt{C_d} < 0.2$  as for the test case with a jet in homogeneous fluid (sec. b). We use open  
 290 boundary conditions on all the boundaries except the inflow where we impose the velocity profile  
 291 of eq. (7). On the lateral boundary, we also use a sponge layer to damp the vertical velocity  
 292 component and the temperature fluctuations. The length of the sponge layer is 5 in the simulations  
 293 with the thin thermocline and 7 in the simulations with the thick thermocline.

294 The mesh used for the stratified case has the same stretching as in the test case of a jet in  
 295 homogeneous fluid in the  $x$  and  $y$  directions, though in a wider domain to be able to capture the  
 296 internal waves propagating in the thermocline. However, we refine the mesh and increase the

297 vertical resolution at the thermocline and in the upper layer of the stratification approximately  
298 up to the penetration height of the fountain to maintain a well-resolved LES. The parameters  
299 pertaining to all simulations are summarized in Table 1, where we also report the case used for the  
300 validation with increased resolution discussed in the Appendix (denoted as 'test'). The resulting  
301 flow is displayed in Fig. 4 for the thick thermocline at  $Fr = 22$ .

302 Validation of our LES model ( $Fr = 13$ , thick thermocline) against the data on weak fountains in  
303 a homogeneous fluid by Lin and Armfield (2000) and experiments on turbulent jets in a stratified  
304 fluid by Ezhova and Troitskaya (2012) is shown in Fig. 3. Fig. 3a shows the decay of the axial  
305 vertical velocity of the jet in the thermocline versus that of the weak fountain in a homogeneous  
306 fluid (Lin and Armfield 2000). Fig. 3b shows several LES profiles of the vertical velocity in  
307 the thermocline and compares them to the experimental data by Ezhova and Troitskaya (2012).  
308 We do not include DNS data for the fountains in this figure since Lin and Armfield (2000) used  
309 an initial parabolic vertical velocity and the vertical velocity profiles tend to keep the parabolic  
310 form in weak fountains; as shown in the figure, the experimental and LES profiles are closer to  
311 Gaussian. Thus, the LES model presented here captures the properties of the mean velocity fields  
312 of the weak fountains.

313 For each simulation we gather statistics (the mean values and the rms of the fluctuations of  
314 all quantities) and save time histories to analyse the jet oscillations and the main features of the  
315 internal waves at specific locations in the flow. We collect statistics approximately 100 time units  
316 after the perturbations at the thermocline have reached the lateral boundary of the computational  
317 domain. This time changes from approximately 900 time units for the thin thermocline and small  
318 Froude number to about 2100 time units for the thick pycnocline and large Froude number. The  
319 duration of the sampling changes from 1200 time units to 4100 time units, with intervals 0.25 time  
320 units for the time histories. To investigate the dynamics of the fountain at the thermocline and



321 the internal waves we examine the oscillations of the isotherm  $T = 0.5$ . The jet oscillations are  
322 characterized by the isotherms at the center of the jet and at 4 points at distance  $r = 1.5$  from the  
323 jet axis, while internal waves are studied by the isotherms corresponding to 2 sets of points located  
324 further away, at  $r = 20$  and  $25$ .

### 325 **3. Results**

326 We shall first examine the statistics of the flow, and, in the following section, consider the inter-  
327 nal waves generated by the interaction between the jet and the thermocline.

#### 328 *a. Jet impingement and entrainment*

329 Fig. 5 shows cross-sections of the absolute value of the mean velocity from our simulations. The  
330 first observation is that the higher the Froude number, the higher the jets penetrate into the ther-  
331 mocline and eventually into the upper layer of stratification. For the lowest  $Fr$  and the strongest  
332 stratification (thin thermocline), the mean flow is reminiscent of a jet impinging on a wall. In the  
333 other cases, the flow has a more complicated structure and a counterflow appears in the thermo-  
334 cline and upper stratification layer to form a fountain. This counterflow is more evident when  
335 increasing the Froude number and decreasing the thickness of the thermocline. The higher the jet  
336 penetrates, the higher the counterflow velocity is and the deeper the annular flow surrounding the  
337 jet propagates into the lower layer. Mixing, in turn, makes the fluid in the counterflow lighter than  
338 the lower layer of stratification, so that it bounces back to the thermocline where it finally spreads  
339 at the level of neutral buoyancy. This structure is characteristic of a two-layer stratification (Cotel  
340 et al. 1997; Ansong et al. 2005) as compared to fountains in homogeneous and linearly strati-  
341 fied media, where the counterflow simply protrudes to the bed or to the level of neutral buoyancy  
342 (Bloomfield and Kerr 1998).

343 To quantify the jet penetration into the thermocline, we report the mean axial jet velocity for all  
 344 the stratified cases and for the turbulent jet in homogeneous medium in Fig. 6a. The evolution in  
 345 the stratified media follows that in a homogeneous medium to  $z \approx 18$ , before the typical behavior  
 346 of a fountain is observed.

347 Fig. 6b reports the penetration heights from the LES defined as the location where the jet velocity  
 348 falls below 1% of the initial velocity.

349 The Froude numbers calculated at the thermocline entrance are characteristic of weak fountains  
 350 and the rising height can be estimated from the conservation of energy (Kaye and Hunt 2006), so  
 351 that the source kinetic energy of the flow is converted into potential energy. This implies:

$$\frac{U_m^2}{2} \sim \int_0^{h_z^*} g a_T (T_s - T_0) dz^*, \quad (12)$$

352 where  $U_m$  is the centreline jet velocity at the level where the fountain is formed (we take  $z^* = 18D$ ),  
 353  $h_z^*$  the penetration height. Normalizing eq. (12) with  $D_0$ ,  $U_0$  and  $\Delta T$  we finally obtain

$$(\lambda u_m)^2 \frac{Fr^2}{2} = \int_0^{h_z} T_s' dz, \quad (13)$$

354 where  $u_m = 0.22$  at  $z = 18$  and  $\lambda$  is a constant of order one which we find from the best fit of  
 355 the LES data. Fig. 6b displays the theoretical dependence of the penetration height obtained  
 356 by integrating eq. (13) with  $\lambda = 0.8$ . The comparison with the LES results indicates that the  
 357 penetration height is well predicted at low Froude numbers but overestimated at the largest  $Fr$ . To  
 358 explain this, we recall that the rising height of weak fountains in a homogeneous fluid scales as  
 359  $Fr^2$  whereas that of forced fountains (where the turbulent entrainment is taken into account) scales  
 360 with  $Fr$ . The largest Froude numbers investigated here correspond to the transition between the  
 361 weak and forced regime, and therefore eq. (12) appropriate for the weak regime overestimates the  
 362 penetration height at these Froude numbers.

363 Note that the theory based on the conservation equations by Morton et al. (1956) is not expected  
364 to be valid for weak fountains near the thermocline because the basic assumptions of the model  
365 about self-similarity and constant turbulent entrainment do not hold. Our calculations show that  
366 this model significantly underestimates the penetration heights from the LES.

367 The dashed lines in Fig. 5 indicate the boundaries of the thermocline (they correspond to 10%  
368 and 90% of the temperature jump) obtained from the average temperature field. It can be seen  
369 that for the thin thermocline and small Froude number (Fig.4a) the temperature jump is deformed  
370 as an entire structure reminiscent of a thick membrane, with variations of the height of the upper  
371 and lower boundaries only in the region of the jet impingement: a strong stratification dampens  
372 turbulence and inhibits mixing. For the higher Froude numbers (Fig. 5b-c) the thin thermocline  
373 is significantly deformed, revealing a toroidal well-mixed region adjacent to the jet. The size and  
374 depth of this well-mixed region grow with the Froude number.

375 Two observations can be made here. Firstly, this behaviour is consistent with the experimental  
376 observations for a turbulent jet impinging on a stratified interface (see, for instance, Shy (1995);  
377 Cotel et al. (1997)) where the formation of a large toroidal vortex was observed immediately after  
378 the jet impingement and related to the generation of baroclinic vorticity which tends to push back  
379 the interface to the unperturbed state. Secondly, which might be more relevant to our system, we  
380 report that the turbulent regime of weak fountains ( $1 \lesssim Fr_t \lesssim 1.9$ ), forming at the thermocline, is  
381 characterized by vertical oscillations of the jet. Here, the fluid falls down quasi periodically from  
382 the top (Troitskaya et al. 2008; Burrige and Hunt 2012; Druzhinin and Troitskaya 2013); these  
383 oscillations are not necessarily axisymmetric, although their average is. The fluid falling from the  
384 top forms the vortical structures adjacent to the jet at the lower boundary of the thermocline. These  
385 structures, together with the small-size eddies on the jet shear layers crossing the thermocline, are  
386 responsible for the turbulent mixing. These large structures and the small eddies on the shear layer

387 are illustrated by the instantaneous fields of temperature and vertical velocity shown in Fig. 7 for  
388 both stratifications and  $Fr = 7$  and  $22$  (i.e.  $Fr_t=0.6$  and  $1.9$ ).

389 The effect of the fountain oscillatory dynamics on the generation of internal waves in the ther-  
390 mocline will be discussed in the next section.

391 To substantiate these observations we study the change of the level of neutral buoyancy with  
392 increasing Froude number, i.e the level where the jet spreads horizontally forming a gravity cur-  
393 rent. This is illustrated by the mean horizontal velocity profiles at the distance  $r = 20$  from the  
394 jet center (Fig. 8a). The vertical coordinate in this picture is  $\eta = \gamma(z - z_p)$ , so that the origin is  
395 moved to the thermocline center and  $\eta = \pm 1$  correspond to the thermocline boundaries. Note that  
396 the width of the horizontal flow is determined by the radius of the jet at the thermocline entrance  
397 which is the same for the two values of thermocline thickness used. In other words, the different  
398 width of the flows in Fig. 8a reflects the different ratio between the thermocline width and the  
399 radius of the impinging jet. For small Froude numbers, the level of neutral buoyancy is below the  
400 lower thermocline boundary while it is moving higher up into the thermocline for larger Froude  
401 numbers, indicating a better mixing with the fluid in the thermocline and from the upper layer of  
402 stratification.

403 To quantify mixing, we calculate the mean temperature of the horizontal flow through the cylin-  
404 drical surface of radius  $r = 20$  surrounding the jet; this distance is chosen so that the control  
405 volume is far enough from the mixing region adjacent to the jet (see Fig. 5,  $15 < z < 25$ ). Using  
406 the mean volume and mass fluxes of the gravity current, we obtain the following expression for  
407 the averaged temperature of the gravity current

$$T_{gr} = \frac{\int T U_{hor} dz}{\int U_{hor} dz} \quad (14)$$

408 where we perform the integration over the region characterized only by positive values of  $U_{hor}$ ,  
 409 i.e. we consider the flow propagating outwards from the jet (detrainment) and do not account  
 410 for entrainment. The values obtained are displayed in Fig. 8b to demonstrate that the average  
 411 temperature of the horizontal flow increases with the Froude number, again indicating a better  
 412 mixing with the fluid in the thermocline and the upper layer of stratification.

413 To study the mixing at the thin and thick thermoclines we introduce the entrainment flux  $E_i =$   
 414  $Q_e/Q_{in}$ , similarly to the definition used for investigations of turbulent entrainment by jets and  
 415 plumes in two-layer (sharp interface) stratified fluid (Shy 1995; Cotel et al. 1997; Shrinivas and  
 416 Hunt 2014, 2015). When the jet penetrates into the upper layer of stratification, it forms a dome-  
 417 like structure which entrains the ambient fluid. Thus  $Q_e$  in the definition above is the volume  
 418 flux of the fluid entrained by the jet top and  $Q_{in}$  is the volume flux of the fluid in the jet at the  
 419 interface between the two layers of stratification. This dome-like structure is reported in Fig. 9,  
 420 where we show the mean horizontal velocity where the jets interact with the thermocline for both  
 421 stratifications under consideration. Since we have a smooth change of temperature between the  
 422 two layers, the 'dome' over which the fluxes are computed is depicted by the black lines in Fig.  
 423 9: we consider a closed surface consisting of a circular cylinder cut on the lower side along the  
 424 surface of the fountain. As the total volume flux is equal to 0, we can estimate the flux through the  
 425 dome perimeter  $Q_e$  as the sum of the fluxes through the cylinder top and side  $Q_{cyl}$ :

$$Q_{cyl} = 2\pi R \int_{z_1}^{z_2} u_{side} dz + 2\pi \int_0^R u_{top} r dr, \quad (15)$$

426 where  $u_{side}$ ,  $u_{top}$  are the velocities normal to the side and top surfaces of the cylinder respectively,  
 427  $z_1, z_2$  are the vertical coordinates corresponding to the bottom and top of the cylinder,  $R$  is the  
 428 radius of the base of the cylinder.

429 We define the inflow volume flux  $Q_{in}$  as the volume flux of the jet at the level  $z = 18$  where it is  
 430 the same for all the cases considered here (see Fig. 6a)

$$Q_{in} = 2\pi \int_0^{\infty} u_{in} r \, dr \quad (16)$$

431 with  $u_{in}$  the vertical velocity. The entrainment flux can finally be written as

$$E_i = \frac{R \int_{z_1}^{z_2} u_{side} \, dz + \int_0^R u_{top} r \, dr}{\int_0^{\infty} u_{in} r \, dr}. \quad (17)$$

432 The dependence of the entrainment flux on the Froude number at the thermocline entrance is  
 433 displayed in Fig. 8c where the dashed curve indicates the theoretical entrainment flux for a jet  
 434 in an unconfined medium in the limit of small Froude numbers ( $Fr_t < 1.4$ ) and a sharp interface,  
 435  $E_i = 0.24Fr_t^2$ , together with the approximation of the theoretical curve for larger Froude numbers,  
 436 both taken from Shrinivas and Hunt (2014). This power law is obtained from an energy balance:  
 437 a fraction of the kinetic energy supplied by the jet at the interface per time unit is expended into  
 438 work (per time unit) against the gravity force to entrain fluid from the upper stratification over a  
 439 distance of the order of the jet scale at the thermocline entrance, yielding  $Q_e/Q_i \sim u_t^2/R_t\Delta g \sim Fr_t^2$   
 440 (here  $u_t$  and  $R_t$  are the mean jet velocity and radius taken at the level of the density interface). The  
 441 value of the constant  $A = 0.24$  is obtained theoretically by Shrinivas and Hunt (2014).

442 Our data follow the quadratic law obtained in Shrinivas and Hunt (2014) for the thin thermocline,  
 443 however, the entrainment rate is slightly higher. Owing to the smoother temperature change in the  
 444 thermocline, the turbulent transfer is expected to be more active in this case than for the sharp  
 445 interface.

446 At small Froude numbers, the fountain in the thick thermocline entrains more fluid although  
 447 the average temperature of the horizontal gravity current is lower. This is due to the fact that  
 448 the jet does not penetrate through the thermocline up to the warm upper layer. At the same time  
 449 the stratification is weaker which results in a larger surface of the dome and more efficient tur-

450 bulent transfer. At higher Froude numbers, when the jet penetrates through the thermocline, the  
451 entrainment fluxes are rather close for the two cases, but the average temperatures for the thick  
452 thermocline are lower.

453 We explain this difference by the presence of a horizontal flow towards the jet in the upper part  
454 of the thick thermocline. In fact, we recall that entrainment velocities (denoted as secondary flows  
455 Shrinivas and Hunt (2015)) play an important role in the process of confined entrainment at small  
456 Froude numbers. As shown in Fig. 9a, the flow above the dome in the thin thermocline looks  
457 similar to the model of a thin "vortex sheet" on the dome perimeter for unconfined entrainment  
458 in a two-layer stratification (Shrinivas and Hunt 2014). Interestingly, a horizontal secondary flow  
459 appears in the thick thermocline. Fig. 9b shows a two-layer horizontal flow in the thermocline.  
460 In this case, stratification inhibits vertical turbulent transfer and the jet entrains the fluid from the  
461 upper thermocline forming a well-pronounced horizontal secondary flow over the initial gravity  
462 current. Even for the largest penetration heights of the jet investigated here, the structure of the  
463 horizontal flow essentially does not change and the jet entrains fluid mostly from the thermocline,  
464 not from the upper stratification layer as in the case of the thin thermocline.

465 Finally, note that the thick thermocline conditions correspond to the experimental setup used  
466 in Troitskaya et al. (2008) and Bondur et al. (2010) to investigate turbulent jets and plumes in  
467 thermocline-like stratified tank. The horizontal velocity profiles measured in the experiments at a  
468 distance  $24R_t$  from the jet center display a back-flow from 6 to 15% of the maximal velocity of the  
469 gravity current in the upper thermocline. Our simulations give a magnitude of 15-20%, at a closer  
470 distance of  $10R_t$ .

471 *b. Generation of internal waves*

472 In all the simulations, as in the experiments of Troitskaya et al. (2008) and Ezhova et al. (2012)  
473 we observe oscillations of the jet top at the thermocline, which results in the generation of internal  
474 waves. An example of the instantaneous temperature field at the center of the thermocline and the  
475 corresponding isotherms at the distance  $r = 20$  from the jet center is shown in Fig. 10 for the case  
476 of the thin thermocline,  $Fr = 10, 22$  ( $Fr_t = 0.86, 1.9$ ). The top figure, pertaining the lower Froude  
477 number, displays rather regular waves emanating from the jet and almost sinusoidal isotherms.  
478 The plots for the larger Froude number show a more chaotic behaviour, the isotherms displaying  
479 signs of wave breaking in the thermocline.

480 The analysis of the dynamics of the jet in the thermocline and of the internal waves is based on  
481 the power spectra of the temperature oscillations. We consider the isotherm at the center of the  
482 undisturbed thermocline,  $T = 0.5$ , and investigate its displacement at several points close to the  
483 jet center and far from it. The spectra of the jet oscillations,  $z - z_p$  with  $z_p$  the average height of  
484 the thermocline  $T = 0.5$ , are obtained by averaging data from 5 locations: one in the center of the  
485 jet and 4 from the points on the circle of radius 1.5 (see Sec. 2c). The spectra of internal waves,  
486 instead, are obtained by averaging spectra from 8 locations at distance  $r = 20$  from the jet center.  
487 The spectra for  $Fr=13$ , thin and thick thermoclines are shown in Fig. 11b, c as an example. It can  
488 be seen that the jet generates internal waves with pronounced spectral peaks.

489 We first note that all the spectra of the jet oscillations in both stratifications have two peaks.  
490 This is consistent with the observation of fountains in a homogeneous fluid where 2 peaks have  
491 been reported for all cases by Burrige and Hunt (2013). Moreover, for fixed  $Fr$ , the spectra of  
492 the jet oscillations have peaks at similar frequencies in different stratifications, as shown in Fig.  
493 11a. Thus, the frequencies of the oscillations do not depend on the thermocline thickness for the



494 parameters chosen in the simulations. Note, however, that one expects differences in frequencies  
 495 when the jet does not penetrate through the thermocline since its effective Froude number is de-  
 496 fined by the temperature difference between the lower stratification layer and the level to which  
 497 jet penetrates, rather than by the difference between upper and lower stratification. In our case this  
 498 difference is probably too small to be detected. Simulations at even lower  $Fr$  may possibly reveal  
 499 this effect.

500 The frequencies of the spectral peaks for jet oscillations and internal waves are summarized in  
 501 Table 2 and displayed in Fig. 12. Since the peaks in the spectra are rather wide we used the  
 502 following expression to define the main frequencies in the spectra:

$$\hat{f} = \frac{\int_{f_{\min}}^{f_{\max}} f \mathcal{S}(f) df}{\int \mathcal{S}(f) df}, \quad (18)$$

503 where  $f_{\min}$  and  $f_{\max}$  denote the range of frequencies corresponding to each spectral peak. The  
 504 figure shows a decrease in the frequency of the oscillations with the Froude number in agreement  
 505 with the fountains in a homogeneous medium (Burridge and Hunt 2013).

506 For the 3 smallest Froude numbers, the spectra of jet oscillations have a pronounced large peak  
 507 and a second small peak at approximately double the frequency. For the 2 highest Froude numbers  
 508 investigated, the peaks have approximately equal magnitude. The spectra of internal waves are dif-  
 509 ferent at lower Froude numbers, with two peaks in the thin thermocline, and one peak in the thick  
 510 thermocline, primarily due to the difference in the maximal buoyancy frequencies as explained  
 511 below.

512 Indeed, the thickness of the two thermoclines considered in this paper corresponds to a factor  
 513 2 difference in the maximal buoyancy frequency. The dimensionless buoyancy frequency,  $N^2 =$   
 514  $g\alpha_T \frac{dT_s}{dz}$ , can be re-written in our case as

$$N^2 = \frac{0.5\gamma}{Fr^2} \frac{1}{\cosh^2(\gamma(z - z_p))}. \quad (19)$$

515 Thus,  $N_{\max} = 1/Fr$  and  $N_{\max} = 0.5/Fr$  for  $\gamma = 2$  and  $\gamma = 0.5$ , respectively. The spectra of jet oscil-  
516 lations and internal waves for the same  $Fr = 13$  and different stratifications are shown in Fig.11b,  
517 c. The spectra of jet oscillations have two distinct peaks, the higher one possibly corresponding to  
518 the harmonics of the lower. The thin thermocline has a larger maximal buoyancy frequency which  
519 allows propagation of waves of both frequencies (first and second peak) while only the lowest fre-  
520 quency perturbation can generate internal waves at the thick thermocline. Fig.12b clearly indicates  
521 the frequency cutoff due to the smaller maximal buoyancy frequency, since the second frequency  
522 in the spectra of the jet oscillations is always higher than the maximum buoyancy frequency for  
523 the thick thermocline.

524 For the 2 higher Froude numbers the spectra of internal waves have one pronounced peak close  
525 to the lower peak of the jet oscillations, which is surprising in case of the thin thermocline where  
526 one expects propagating waves at both frequencies. The simulations for these cases, when the jet  
527 penetrates far enough through the thermocline, show that fluid falling from the jet top loses axial  
528 symmetry, in contrast to the cases at smaller Froude numbers, and the jet undergoes 'tilting' from  
529 one side to the other. This may explain why internal waves propagate only at the low frequency.  
530 Moreover, the fluid falling from the fountain goes deep to the lower layer of stratification and then  
531 bounces back creating additional disturbances in the thermocline which might result in a frequency  
532 shift. This is more relevant for the thin thermocline where we see a more pronounced shift of the  
533 frequency of the internal waves from the lower peak in the spectra of the jet oscillations (Fig. 12a).

534 In case of the thin thermocline, the frequency of the higher peak in the spectra of the internal  
535 waves decreases from  $0.5N_{\max}$  to  $0.3N_{\max}$ . For the thick thermocline the peak in the spectrum  
536 of the internal waves corresponds to the lower peak in the jet oscillations spectrum and is close  
537 to  $0.7N_{\max}$  for all the simulations. The latter is consistent with the results of the experiment by  
538 Ezhova et al. (2012) where the oscillations of a turbulent jet in a stratified fluid and the corre-

539 sponding internal waves have been investigated. As mentioned before, the jet diameter at the ther-  
540 mocline entrance was of order of the thermocline thickness in these experiments corresponding  
541 to our simulations with the thick thermocline,  $Fr_t \sim 1$ . In the experiments, the jet oscillations are  
542 characterized by pronounced peaks close to  $0.7N_{\max}$  and at the frequency close to the maximum  
543 buoyancy frequency. Internal waves have been revealed at the frequencies  $0.7N_{\max}$  in agreement  
544 with our simulations.

545 The root mean square  $\sigma$  of the isotherms both for jet oscillations and internal waves, i.e. close  
546 and far from the jet axis, is obtained from the power spectra,  $\mathcal{S}(f)$ ,

$$\sigma = \left( \int \mathcal{S}(f) df \right)^{1/2}, \quad (20)$$

547 and used to characterize the amplitudes of the oscillations. The amplitudes of the jet oscillations  
548 and internal waves are displayed in Fig.13a versus the Froude number for both stratifications.  
549 Interestingly, the amplitudes of the jet oscillations and of the internal waves are close to each other  
550 in both cases, although the work against gravity force to obtain the same amplitude is larger in  
551 the thin thermocline as the density gradient is higher. This suggests that the waves are transmitted  
552 more effectively in the case of the thin thermocline, probably due to the fact that for the thick  
553 thermocline the wave frequency is close to the maximal buoyancy frequency.

554 The amplitude of the jet oscillations follows the stationary solution to the Landau equation

$$\frac{d\sigma}{dt} = \sigma(\mu(Fr_t - Fr_{t0}) - \beta\sigma^2) \quad (21)$$

555 describing the soft excitation of self-sustained oscillations ( $\mu$  and  $\beta$  are free parameters here) with  
556  $Fr_{t0} = 0.4$ ,  $\mu/\beta = 0.42$  based on the best fit of the experimental data. This is consistent with  
557 the experimental and numerical results obtained for a jet interacting with a pycnocline (Troitskaya  
558 et al. 2008; Druzhinin and Troitskaya 2013). The investigation of the stability of the experi-  
559 mentally measured velocity profiles of the fountain in the pycnocline by Troitskaya et al. (2008);

560 Ezhova and Troitskaya (2012) reveals a finite region of absolute instability along the jet, thus ful-  
 561 filling a necessary condition for self-sustained oscillations of the flow. It has been demonstrated  
 562 that the frequency of self-sustained oscillations is in agreement with the results of the linear sta-  
 563 bility analysis of the flow in the thermocline. The present simulations for the thick thermocline  
 564 follow the experimental setup of Ezhova and Troitskaya (2012) and the LES results are consistent  
 565 with the experiment. Hence, we can conclude that the generation of internal waves results from  
 566 the self-sustained excitation of the jet oscillations in the thermocline.

567 We investigate the vertical structure of the internal waves and quantify their energetics. The  
 568 energy flux of the internal waves in the presence of an inhomogeneous horizontal flow, as we  
 569 have in this case because of the horizontal gravity flow, is calculated following Kamenkovich and  
 570 Monin (1978). The equations of motion linearised around a horizontal mean flow in cylindrical  
 571 coordinates are:

$$\frac{Du'_r}{Dt} + u'_z \frac{dU_{hor}}{dz} + \frac{1}{\rho_0} \frac{\partial p'}{\partial r} = 0, \quad (22)$$

$$\frac{Du'_\phi}{Dt} + \frac{1}{\rho_0} \frac{1}{r} \frac{\partial p'}{\partial \phi} = 0, \quad (23)$$

$$\frac{Du'_z}{Dt} + g \frac{\rho'}{\rho_0} + \frac{1}{\rho_0} \frac{\partial p'}{\partial z} = 0, \quad (24)$$

$$g \frac{D(\rho'/\rho_0)}{Dt} - N^2(z) u'_z = 0, \quad (25)$$

$$\nabla \cdot \vec{u}' = 0, \quad (26)$$

572 where  $D/Dt = \frac{\partial}{\partial t} + U_{hor} \frac{\partial}{\partial r}$ .

573 The equation for energy conservation can be obtained by multiplying Eq. (22) with  $u'_r$ , Eq. (23)  
 574 by  $u'_\phi$ , Eq. (24) by  $u'_z$  and summing. From Eq. (25), taking into account that  $u'_z = \frac{D\xi}{Dt}$ , we find  
 575 that  $g\rho' = \rho_0 N^2(z)\xi$  (where  $\xi$  is the vertical displacement of a fluid particle).

576 Finally, the equation of the wave energy conservation reads:

$$\frac{\partial E}{\partial t} + \nabla \vec{F} = -I, \quad (27)$$

577 where the wave energy  $E$ , the energy flux  $\vec{F}$  and the production/dissipation term  $I$  are

$$E = \frac{1}{2} \rho_0 (\vec{u}'^2 + N^2 \xi^2), \quad (28)$$

$$\vec{F} = \vec{U}_{hor} E + \vec{u}' p', \quad (29)$$

$$I = \rho_0 u'_r u'_z \frac{dU_{hor}}{dz}. \quad (30)$$

578 The term  $I$  describes the interaction of the mean flow with the wave. From equation (27) it  
 579 follows that the integral wave energy flux is not conserved due to this term. In the present config-  
 580 uration, waves can grow or decay in space where  $\frac{\partial E}{\partial t}$  is zero at statistically steady state.

581 The surface-integrated value of the wave energy flux at the distance  $r$  from the jet axis is nor-  
 582 malized with the energy flux of the jet at the thermocline entrance,

$$\frac{F}{F_{jet}} = \frac{R \int_{z_1}^{z_2} \left( \frac{1}{2} (\vec{u}'^2 + N^2 \xi^2) U_{hor} + \frac{p' u'_r}{\rho_0} \right) dz}{\frac{1}{2} \int_0^\infty U_t^3 r dr}. \quad (31)$$

583 We measure the profiles of the energy flux at 4 radial points and averaged them to get the final  
 584 profile. The inflow energy flux is taken at the level  $z = 18$ . The profiles  $\frac{F}{F_{jet}}$  pertaining the thick  
 585 and thin thermocline at the distances  $r = 20$  and  $r = 25$  are shown in Fig. 14. It can be seen  
 586 that the energy does not only decay with the distance from the jet centre, but the profiles are also  
 587 deformed, especially in the areas affected by the shear due to the horizontal flow, presumably due  
 588 to the enhanced decay resulting from the interaction with the mean flow.

589 The surface-integrated wave energy flux normalized with the jet energy flux is displayed in Fig.  
 590 15 versus the Froude number. The difference between the values at  $r = 20$  and  $r = 25$  illustrates  
 591 the difference in the decay of the energy of the internal waves due to the interaction with the

592 mean flow. Note that the wave energy flux is around 4-5% of the energy of the jet for the thin  
 593 thermocline, and is almost half for the thick thermocline. This can be partly explained by the  
 594 fact that the counterflow in the upper thermocline transfers energy in the opposite direction, i.e.  
 595 towards the jet. The whole flux, however, is always positive. Note also the jump in the energy flux  
 596 for the largest Froude number when the horizontal flow occupies more space in the thermocline  
 597 preventing the transfer of energy towards the jet.

598 We finally comment on the difference in the velocities of wave propagation. As explained above,  
 599 transients in the simulations are very different when changing the thickness of the thermocline, and  
 600 the difference in the domain size (40 from the jet center to the lateral boundary along the axes for  
 601 the thin thermocline, and 47 for the thick thermocline) is too small to explain this. The fact that  
 602 the internal waves are significantly slower in the thick thermocline can be related to the dispersion  
 603 properties of the internal waves. The dispersion relation for the waves  $\Psi \sim \psi(z)e^{-i\omega t + ikr}$  in a  
 604 stratified medium is obtained from the solution of the eigenvalues of the Taylor-Goldstein equation

$$\frac{d^2\psi}{dz^2} + \left( \frac{N^2}{(U_{hor} - c)^2} - \frac{(U_{hor})''_{zz}}{U_{hor} - c} - k^2 \right) \psi = 0, \quad \psi(H_d) = \psi(H_u) = 0, \quad (32)$$

605 where  $\psi$  is a stream function,  $N$  the buoyancy frequency,  $U_{hor}$  the mean horizontal velocity which  
 606 depends on the vertical coordinate  $z$ ,  $c = \omega/k$  the wave phase velocity ( $\omega$  is the wave frequency,  $k$   
 607 is the wave number), and  $z = H_u, H_d$  denote the locations of the upper and lower boundaries (eq.  
 608 (32) is made non-dimensional with  $U_0$  and  $D_0$ ). This eigenvalue problem is solved numerically for  
 609 the stratification profiles and the horizontal velocities extracted from the simulations.

610 The group velocity,  $c_g = d\omega/dk$ , of the first (fundamental) mode of the internal waves is dis-  
 611 played in Fig.13b for the Froude numbers  $Fr = 0$  (no flow) and  $Fr = 13$  (with horizontal flow)  
 612 and both stratifications. Similar conclusions apply to higher modes. Note the significant change  
 613 in the group velocities in the presence of the horizontal flow due to the jet intrusion at the level of

614 neutral buoyancy. In particular, we find waves with frequencies higher than the maximal buoyancy  
615 frequency that propagate with group velocities approaching the maximal velocity of the horizontal  
616 gravity flow. The largest fluctuations associated to these modes are localized in the flow as com-  
617 pared to the lower frequency modes localized in the thermocline. For the internal waves at  $Fr = 13$   
618 (see the frequencies in Table 2) we estimate the group velocities of the fundamental modes to be  
619  $c_{gr} = 0.04$  for the thick thermocline and  $c_{gr} = 0.08$  for the thin thermocline, which explains the  
620 difference in time needed to reach a statistically steady state,  $t_{d,thin} = 1000$  and  $t_{d,thick} = 1800$ .

#### 621 4. Conclusion

622 We have presented the results of numerical simulations of a turbulent jet interacting with a ther-  
623 mocline in an unconfined stratified medium. Two stratifications have been modelled: a thin and  
624 a thick thermocline, with thickness smaller and of the order of the jet diameter at the thermocline  
625 entrance. The simulations have been performed for 5 Froude numbers in each stratification, rang-  
626 ing between 0.6 and 1.9, values typical of engineering and geophysical flows, such as submerged  
627 buoyant jets from wastewater outfalls.

628 We show that the jet mean penetration height can be well predicted from the conservation of the  
629 source energy of a turbulent jet in a thermocline (Kaye and Hunt 2006), valid for weak fountains.

630 The entrainment flux in the thin thermocline, related to the turbulent mixing of the jet with the  
631 surrounding medium, is consistent with the theoretical model developed for the case of a jet im-  
632 pinging at a sharp interface. At small Froude numbers, the entrainment is more effective in the  
633 thick thermocline, but already at  $Fr_t \approx 1$  the fluxes become equal for both stratifications. There is  
634 an important difference, however, in the average secondary flows for the two stratifications. For  
635 the thin thermocline the entrainment velocity is approximately the same around the 'dome' formed  
636 by the jet penetrating through the thermocline. The entrainment in the thick thermocline, instead,

637 is mostly from the sides of the 'dome' due to a pronounced horizontal flow in the upper thermo-  
638 cline, with only a small part of fluid coming from the upper stratification layer. This difference is  
639 observed over the whole range of Froude numbers investigated here, even in the case when the jet  
640 penetrates through the thick thermocline.

641 The fountain formed by the jet penetrating into the thermocline oscillates generating internal  
642 waves. The amplitudes of the jet oscillations grow with the Froude number as  $Fr_t^{1/2}$  corresponding  
643 to the regime of soft self-excitation of the flow. We find two peaks in all the spectra: for the smaller  
644 Froude numbers (up to  $Fr_t \approx 1$ ) the peak at the higher frequency is rather weak as compared to the  
645 second one, while at the larger Froude numbers they are comparable. The frequencies of the jet  
646 oscillations at fixed  $Fr_t$  are basically the same for both stratifications. These oscillations generate  
647 internal waves. The frequencies of the internal waves depend also on the dispersion properties of  
648 the stratified medium and oscillations at frequency exceeding maximal buoyancy frequency are  
649 not found in the spectra of internal waves. Therefore, at the lower Froude numbers both peaks are  
650 present in the spectra of internal waves in case of the thin thermocline while only one peak in the  
651 thick thermocline.

652 At the higher Froude numbers there is one pronounced peak in the spectra of internal waves  
653 corresponding approximately to the lower peak in the spectra of jet oscillations. This is consistent  
654 with the results of the laboratory experiments of Troitskaya et al. (2008) and Ezhova et al. (2012),  
655 corresponding to our simulations with the thick thermocline at  $Fr_t \approx 1$ .

656 The energy flux of internal waves at the thermocline entrance is estimated to be around 4-5%  
657 of the jet energy for the thin thermocline at the distance  $r = 20$  from the jet center, and almost  
658 half for the thick thermocline, except for the largest Froude number,  $Fr_t = 1.89$ , when the fluxes  
659 are equal. The energy profiles and estimates of the energy flux at the distance  $r = 25$  show that  
660 internal waves are significantly influenced by the horizontal gravity flow.



661 We finally make some remarks regarding a possible application of the present numerical results  
662 to the wastewater outfall system. As in the scale laboratory modelling of the real system (Troit-  
663 skaya et al. 2008), we have observed the jet oscillations resulting in the generation of internal  
664 waves at a frequency close to  $0.7N_{\max}$  for the thick thermocline cases. These waves can be rather  
665 strong with an average amplitude up to 20% of the thermocline thickness (40% peak-to-peak) at  
666 the distance of 5 thermocline thicknesses from the source. The seasonal change of the pycnocline,  
667 as we briefly discussed in the Introduction, is characterized primarily by its sharpening and its tran-  
668 sition closer to the surface. Therefore, at the entrance to the thermocline, the diameter of the jet  
669 increases and the vertical velocity decreases, i.e. increasing  $\gamma_l$  and decreasing the Froude number  
670 at the thermocline entrance. Hence we expect that in summer, due to the lower  $Fr_l$  and amplitude,  
671 the internal waves, albeit closer to the free surface, generate less mixing and the entrainment at  
672 the top of the jet be less effective than in winter. The waste water effluent will be located closer  
673 to the free surface and its dilution will be reduced in summer, presenting a larger threat than in  
674 winter when a more effective entrainment and larger amplitude internal waves will contribute to  
675 the dilution of the effluent trapped further away from the free surface. Better dilution is expected  
676 either due to the possible wave breaking or due to the effect of enhancement of turbulence in the  
677 field of a non-breaking internal wave (Matusov et al. (1989), Druzhinin and Ostrovsky (2015)).

678 This study focuses on turbulent jets generated from a momentum source of fluid of the same  
679 density as the surrounding ambient fluid. The investigation of the applicability of the results  
680 discussed in this paper to a turbulent plume with a finite buoyancy flux is underway. However,  
681 if the results presented hold for a plume with a finite buoyancy flux, we expect that the different  
682 stratification observed in summer and winter in tidewater glaciers in Greenland (Straneo et al.  
683 2011) will influence dramatically the formation and propagation of internal waves in this setting.  
684 In particular, in winter, the interface between the top and bottom layers in some of Greenland's

685 fjords is sharp and thinner than in summer (Straneo et al. 2011) and the buoyant plumes forming at  
686 the glacier face due to submarine melting are weaker due to a low (or absent) subglacial discharge.  
687 Hence, we expect the lower  $Fr_t$  and thinner interface observed in winter to generate low amplitude  
688 internal waves with two spectral peaks and the entrainment at the top of the plume to be less  
689 effective than in summer when the Froude number is larger. Additionally in summer, given the  
690 larger  $Fr_t$  and thicker interface, the buoyant plumes interacting with the interface are expected to  
691 generate large amplitude internal waves which can possibly break and contribute to the dilution of  
692 the meltwater plume intruding horizontally at the interface.

693 *Acknowledgments.* This work was supported by the Linné FLOW Centre at KTH, the European  
694 Research Council Grant No. ERC-2013-CoG-616186, TRITOS, and the Swedish Research Coun-  
695 cil (VR), Outstanding Young Researcher Award. Support to C.C. was given by the NSF project  
696 OCE-1434041. Computer time was provided by SNIC (Swedish National Infrastructure for Com-  
697 puting). Visualization and graphic analysis were performed with VisIt (Childs et al. 2012) and  
698 Gnuplot. Subroutines used in the numerical models are available from Numerical Analysis library  
699 of RCC MSU.

## 700 APPENDIX

### 701 **Convergency test and additional validations**

702 We investigate the sensitivity of the simulations to the size of spectral elements. For this aim  
703 we perform an additional simulation for  $Fr = 13$ , thin pycnocline, with an increased resolution.  
704 We left the size of the well-resolved initial region at the inflow ( $4 \times 4 \times 10$  spectral elements)  
705 unaffected in order to keep the same velocity perturbations and obtain the turbulent jet with the  
706 same characteristics. However, we reduce stretching factor to have 2 times smaller elements at

707  $|x| = |y| = 10$  and reduced the stretching factor along  $z$ -axis to have twice more elements in the  
708 thermocline. The meshes for both cases are shown in Fig. A1a,b displaying as an example the  
709 instantaneous temperature fields for both simulations.

710 Fig. A1d,e shows the average velocity fields together with the thermocline boundaries for both  
711 cases indicating good correspondence. The jet centerline velocity as the function of the vertical  
712 coordinate illustrating mean jet penetration is shown in Fig. A1c. The entrainment flux for the test  
713 case is  $E_{i,test} = 0.36$  as compared to the regular grid with  $E_i = 0.37$ . Thus we may conclude that  
714 the simulations converge and the calculations are resolved enough to get reliable results.

715 One can investigate the influence of reflections from the boundaries comparing the internal  
716 waves measured at the distances  $r = 20$  and  $r = 25$ . We expect to get the weaker signal at  $r = 25$   
717 and delay with respect to  $r = 20$ .

718 The examples of the isotherms for the largest Froude numbers, as the most critical case for  
719 reflections, are shown in Fig. A2 for both stratifications. Fig. A2 displays also the averaged  
720 spectra of internal waves measured at  $r = 20$  and  $r = 25$  (averaging performed over 8 realizations  
721 as explained in Sec. 2 b). It can be seen that the signals at  $r = 25$  follow the signals at  $r = 20$ . The  
722 average spectra of the isotherms are similar but the peak for  $r = 25$  is lower thus confirming the  
723 absence of reflections from the boundaries at  $r = 20$  where we measure internal waves.

## 724 **References**

- 725 Ansong, J. K., P. J. Kyba, and B. R. Sutherland, 2005: Fountains impinging on a density interface.  
726 *J. Fluid Mech.*, **595**, 115–139.
- 727 Ansong, J. K., and B. R. Sutherland, 2010: Internal gravity waves generated by convective plumes.  
728 *J. Fluid Mech.*, **648**, 405–434.

- 729 Bloomfield, L. J., and R. C. Kerr, 1998: Turbulent fountains in a stratified fluid. *J. Fluid Mech.*,  
730 **358**, 335–356.
- 731 Bloomfield, L. J., and R. C. Kerr, 2000: A theoretical model of a turbulent fountain. *J. Fluid*  
732 *Mech.*, **424**, 197–216.
- 733 Bondur, V. G., Y. V. Grebenyuk, E. V. Ezhova, V. I. Kazakov, D. A. Sergeev, I. A. Soustova, and  
734 Y. I. Troitskaya, 2010: Surface manifestations of internal waves investigated by a subsurface  
735 buoyant jet: 2. Internal waves field. *Izvestiya, Atmospheric and Oceanic Physics*, **46**, 347–359.
- 736 Burridge, H. C., and G. R. Hunt, 2012: The rise heights of low- and high-Froude-number turbulent  
737 axisymmetric fountains. *J. Fluid Mech.*, **691**, 392–416.
- 738 Burridge, H. C., and G. R. Hunt, 2013: The rhythm of fountains: the length and time scales of rise  
739 height fluctuations at low and high Froude numbers. *J. Fluid Mech.*, **728**, 91–119.
- 740 Childs, H., and Coauthors, 2012: VisIt: An End-User Tool For Visualizing and Analyzing Very  
741 Large Data. *High Performance Visualization—Enabling Extreme-Scale Scientific Insight*, 357–  
742 372.
- 743 Cotel, A. J., J. A. Gjestvang, N. N. Ramkhelavan, and R. E. Breidenthal, 1997: Laboratory experi-  
744 ments of a jet impinging on a stratified interface. *Exps Fluids*, **23**, 155–160.
- 745 Druzhinin, O. A., and L. A. Ostrovsky, 2015: Dynamics of turbulence under the effect of stratifi-  
746 cation and internal waves. *Nonlin. Proc. Geophys.*, **22**, 337–348.
- 747 Druzhinin, O. A., and Y. I. Troitskaya, 2012: Regular and chaotic dynamics of a fountain in a  
748 stratified fluid. *CHAOS*, **22**, 023116.
- 749 Druzhinin, O. A., and Y. I. Troitskaya, 2013: Internal wave radiation by a turbulent fountain in a  
750 stratified fluid. *Fluid Dynamics*, **48**, 827–836.

751 Ezhova, E. V., D. A. Sergeev, A. A. Kandaurov, and Y. I. Troitskaya, 2012: Nonsteady dynam-  
752 ics of turbulent axisymmetric jets in a stratified fluid: Part 1. Experimental study. *Izvestiya,*  
753 *Atmospheric and Oceanic Physics*, **48**, 409–417.

754 Ezhova, E. V., and Y. I. Troitskaya, 2012: Nonsteady dynamics of turbulent axisymmetric jets in  
755 a stratified fluid: Part 2. Mechanism of excitation of axisymmetric oscillations in a submerged  
756 jet. *Izvestiya, Atmospheric and Oceanic Physics*, **48**, 528–537.

757 Fischer, P. F., J. W. Lottes, and S. G. Kerkemeier, 2008: Nek5000 Web pages.  
758 <http://nek5000.mcs.anl.gov>.

759 Friedman, P. D., 2006: Oscillations in height of a negatively buoyant jet. *Trans. ASME J.: J. Fluids*  
760 *Engng*, **128**, 880–882.

761 Friedman, P. D., V. D. Vadokoot, W. J. Meyer, and S. Carey, 2007: Instability threshold of a  
762 negatively buoyant fountain. *Exps Fluids*, **42**, 751–759.

763 Germano, M., U. Piomelli, P. Moin, and W. H. Cabot, 1991: A dynamic subgrid-scale eddy vis-  
764 cosity model. *Phys. Fluids A*, **9**, 1760–1765.

765 Hunt, J. C. R., 1994: Atmospheric jets and plumes. *Recent Research Advances in the Fluid Me-*  
766 *chanics of Turbulent Jets and Plumes*, P. A. Davies, and M. J. Valente Neves, Eds., Kluwer  
767 Academic Publishers, 309–334.

768 Hussein, J., S. P. Capp, and W. K. George, 1994: Velocity measurements in a high-Reynolds-  
769 number momentum-conserving, axisymmetric turbulent jet. *J. Fluid Mech.*, **258**, 31–75.

770 Jirka, G. H., and J. H. W. Lee, 1994: Waste disposal in the ocean. *Water quality and its control*,  
771 M. Hino, Ed., Balkema, Rotterdam, 193–242.

- 772 Kamenkovich, V. M., and A. S. Monin, 1978: *Ocean Physics, Vol. 1*. Moscow, Nauka Publishing  
773 House.
- 774 Kaye, N. B., and G. R. Hunt, 2006: Weak fountains. *J. Fluid Mech.*, **558**, 319–328.
- 775 Knauss, J., 2005: *Introduction to Physical Oceanography, 2nd Edition*. Waveland Press.
- 776 Lin, W., and S. W. Armfield, 2000: Direct simulation of weak axisymmetric fountains in a homo-  
777 geneous fluid. *J. Fluid Mech.*, **403**, 67–88.
- 778 Lin, Y. J. P., and P. F. Linden, 2005: The entrainment due to a turbulent fountain at a density  
779 interface. *J. Fluid Mech.*, **542**, 25–52.
- 780 List, E. J., 1982: Turbulent jets and plumes. *Annu. Rev. Fluid Mech.*, **26**, 189–212.
- 781 Matusov, P. A., L. A. Ostrovsky, and L. S. Tsimring, 1989: Amplification of small scale turbulence  
782 by the internal waves. *Dokl. Acad. Sci. USSR*, **307**, 979–984.
- 783 McDougall, T. J., 1981: Negatively buoyant vertical jets. *Tellus*, **33**, 313–320.
- 784 Morton, B. R., G. Taylor, and J. S. Turner, 1956: Turbulent gravitational convection from main-  
785 tained and instantaneous sources. *Proc. Royal Soc. London, Series A*, **234**, 1–25.
- 786 Ohlsson, J., P. Schlatter, P. F. Fischer, and D. S. Henningson, 2010: Large eddy simulation of  
787 turbulent flow in a plane asymmetric diffuser by the spectral element method. *Direct and Large*  
788 *Eddy Simulation VII*, 197–204.
- 789 Orlandy, I., 1976: A simple boundary condition for unbounded hyperbolic flows. *J. Comput.*  
790 *Phys.*, **21**, 251–269.
- 791 Panchapakesan, N. R., and J. L. Lumley, 1993: Turbulence measurements in axisymmetric jets of  
792 air and helium. Part 1. Air jet. *J. Fluid Mech.*, **256**, 197–223.

- 793 Pham, M. V., F. Plourde, and S. K. Doan, 2007: Direct and large-eddy simulations of a pure  
794 thermal plume. *Phys. Fluids*, **19**, 125103.
- 795 Pham, M. V., F. Plourde, S. K. Doan, and S. Balachandar, 2006: Large eddy simulation of a pure  
796 thermal plume under rotating conditions. *Phys. Fluids*, **18**, 015101.
- 797 Picano, F., and C. S. Casciola, 2007: Small-scale isotropy and universality of axisymmetric jets.  
798 *Phys. Fluids*, **19**, 118106.
- 799 Picano, F., and K. Hanjalic, 2012: Leray- $\alpha$  regularization of the Smagorinsky-closed filtered equa-  
800 tions for turbulent jets at high Reynolds numbers. *Flow Turbulence Combust.*, **89**, 627–650.
- 801 Pope, S., 2000: *Turbulent flows*. Cambridge University Press.
- 802 Sciascia, R., F. Straneo, C. Cenedese, and P. Heimbach, 2013: Seasonal variability of submarine  
803 melt rate and circulation in an East Greenland fjord. *J. Geophys. Res.*, **118**, 2492–2506.
- 804 Shrinivas, A. B., and G. R. Hunt, 2014: Unconfined turbulent entrainment across density inter-  
805 faces. *J. Fluid Mech.*, **757**, 573–598.
- 806 Shrinivas, A. B., and G. R. Hunt, 2015: Confined turbulent entrainment across density interfaces.  
807 *J. Fluid Mech.*, **779**, 116–143.
- 808 Shy, S. S., 1995: Mixing dynamics of jet interaction with a sharp density interface. *Exp. Therm.*  
809 *Fluid Sci.*, **10**, 355–369.
- 810 Smagorinsky, J., 1963: General circulation experiments with the primitive equations. *Mon.*  
811 *Weather Rev.*, **91**, 99–164.
- 812 Stewart, R. H., 2008: *Introduction to Physical Oceanography*. Texas A& M University.

- 813 Straneo, F., and C. Cenedese, 2015: Dynamics of Greenlands glacial fjords and their role in cli-  
814 mate. *Annu Rev Marine Sci*, **7**, 89–112.
- 815 Straneo, F., R. Curry, D. Sutherland, G. Hamilton, C. Cenedese, K. Vage, and L. Stearns, 2011:  
816 Impact of fjord dynamics and glacial runoff on the circulation near Helheim Glacier. *Nature*  
817 *Geophysics*, **4**, 322–327.
- 818 Troitskaya, Y. I., D. A. Sergeev, E. V. Ezhova, I. A. Soustova, and V. I. Kazakov, 2008: Self-  
819 induced internal waves excited by buoyant plumes in a stratified tank. *Doklady Earth Sci.*, **419**,  
820 506–510.
- 821 Turner, J. S., 1966: Jets and plumes with negative or reversing buoyancy. *J. Fluid. Mech.*, **26**,  
822 779–792.
- 823 Turner, J. S., 1973: *Buoyancy effects in Fluids*. Cambridge University Press.
- 824 Williamson, N., N. Srinarayana, S. W. Armfield, G. D. McBain, and W. Lin, 2008: Low-Reynolds-  
825 number fountain behaviour. *J. Fluid Mech.*, **608**, 297–317.



826 **LIST OF TABLES**

827 **Table 1.** Parameters of the simulations of a jet impinging on a thin or thick thermocline.  
 828 The nominal Froude number is  $Fr = U_0/\sqrt{g'D_0}$ , while the thermocline Froude  
 829 number  $Fr_t = u_t/\sqrt{g'R_t}$  uses the jet mean radius and velocity at  $z = 18$  (for  
 830 comparison with Shrinivas and Hunt (2014, 2015)),  $\gamma = D_0/H$  indicates the  
 831 inverse thickness of the thermocline. . . . . 40

832 **Table 2.** Frequencies of jet oscillations and internal waves in the thin and thick thermo-  
 833 clines. . . . . 41

834 TABLE 1. Parameters of the simulations of a jet impinging on a thin or thick thermocline. The nominal  
835 Froude number is  $Fr = U_0/\sqrt{g'D_0}$ , while the thermocline Froude number  $Fr_t = u_t/\sqrt{g'R_t}$  uses the jet mean  
836 radius and velocity at  $z = 18$  (for comparison with Shrinivas and Hunt (2014, 2015)),  $\gamma = D_0/H$  indicates the  
837 inverse thickness of the thermocline.

$Fr, Fr_t$	$\gamma = D/H$	Domain Size	N. Spectral Elements	N. of Grid Points
7 (0.60)	2	$80 \times 80 \times 31$	$38 \times 38 \times 36$	26 615 808
10 (0.86)	2	$80 \times 80 \times 31$	$38 \times 38 \times 36$	26 615 808
13 (1.11)	2	$80 \times 80 \times 32$	$38 \times 38 \times 38$	28 094 464
test 13 (1.37)	2	$80 \times 80 \times 32$	$48 \times 48 \times 45$	53 084 160
16 (1.37)	2	$80 \times 80 \times 33$	$38 \times 38 \times 42$	31 051 776
22 (1.89)	2	$95 \times 95 \times 37$	$40 \times 40 \times 52$	42 598 400
7 (0.60)	0.5	$95 \times 95 \times 32.5$	$40 \times 40 \times 33$	27 033 600
10 (0.86)	0.5	$95 \times 95 \times 33.5$	$40 \times 40 \times 35$	28 672 000
13 (1.11)	0.5	$95 \times 95 \times 34.5$	$40 \times 40 \times 36$	29 491 200
16 (1.37)	0.5	$95 \times 95 \times 35.5$	$40 \times 40 \times 37$	30 310 400
22 (1.89)	0.5	$95 \times 95 \times 40.5$	$40 \times 40 \times 45$	36 364 000

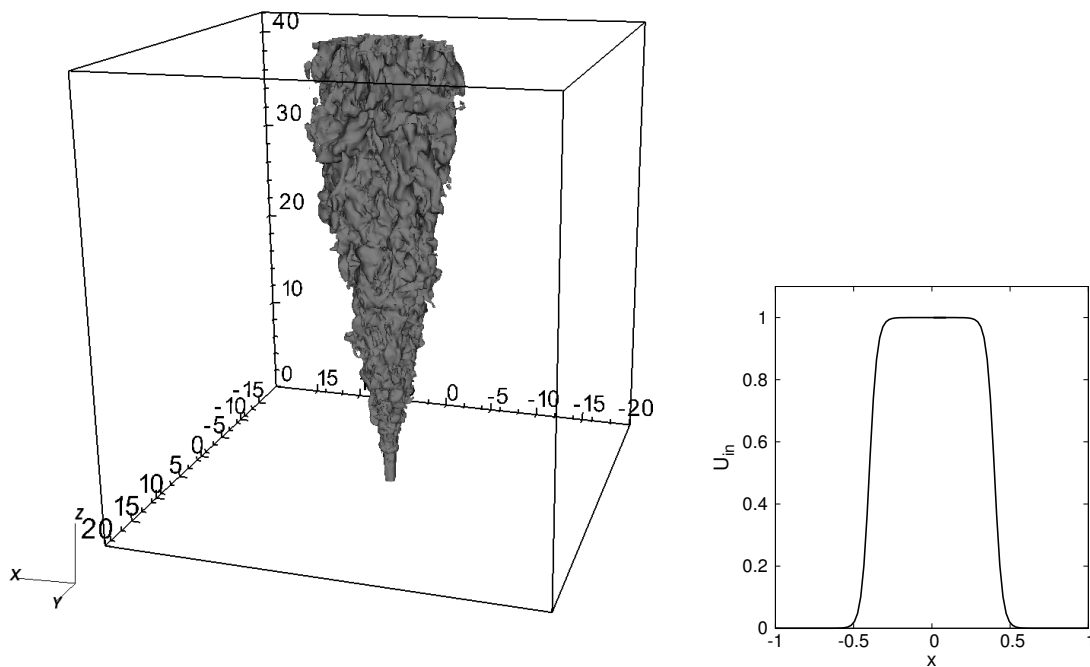
TABLE 2. Frequencies of jet oscillations and internal waves in the thin and thick thermoclines.

$Fr(Fr_t)$	$\hat{f}_{1jet}$ thin	$\hat{f}_{2jet}$ thin	$\hat{f}_{1jet}$ thick	$\hat{f}_{2jet}$ thick	$\hat{f}_{1IW}$ thin	$\hat{f}_{2IW}$ thin	$\hat{f}_{1IW}$ thick
7 (0.60)	0.0096	0.0179	0.0098	0.0177	0.0100	0.0173	0.0083
10 (0.86)	0.0072	0.0146	0.0068	0.0152	0.0078	0.0135	0.0063
13 (1.11)	0.0038	0.0082	0.0042	0.0084	0.0040	0.0073	0.0045
16 (1.37)	0.0024	0.0055	0.0026	0.0054	0.0037	-	0.0030
22 (1.89)	0.0017	0.0048	0.0021	0.0048	0.0023	-	0.0025

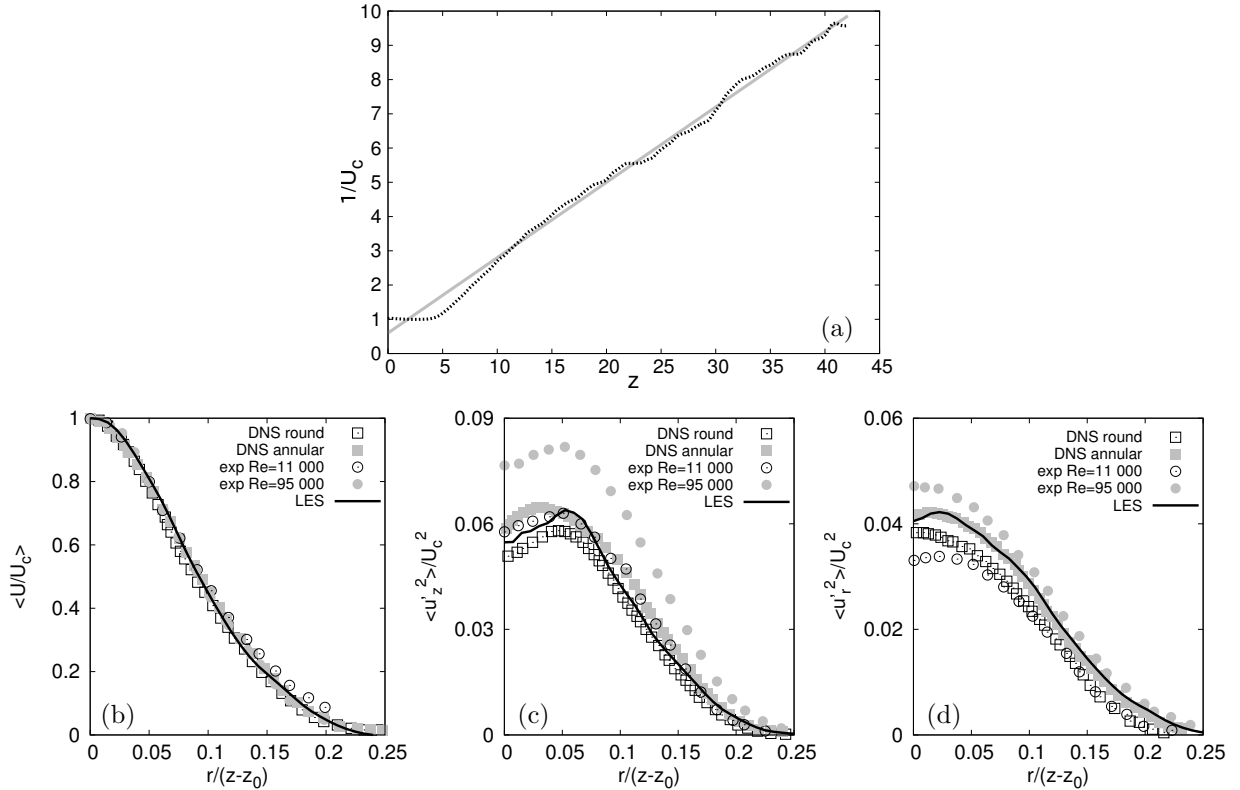
## LIST OF FIGURES

838		
839	<b>Fig. 1.</b>	Left panel: domain configuration for the turbulent jet in a homogeneous fluid. The jet is shown by the contour surface of vertical velocity $u_z = 0.03$ . Right panel: an inflow velocity profile. . . . . 44
840		
841		
842	<b>Fig. 2.</b>	(a) Inverse mean centerline velocity as a function of the distance from the nozzle (black dots - LES data, gray - theory). (b) The far-field $z$ -velocity profile, (c) turbulent stresses $\langle u_z'^2 \rangle / U_c^2$ and (d) $\langle u_r'^2 \rangle / U_c^2$ . The data for comparison are available from the following papers: 'DNS round' - Picano and Casciola (2007), 'DNS annular' - Picano and Hanjalic (2012), 'exp Re=11 000' - Panchapakesan and Lumley (1993), 'exp Re=95 000' - Hussein et al. (1994). . . . . 45
843		
844		
845		
846		
847		
848	<b>Fig. 3.</b>	Comparison of present LES data with direct numerical simulations (DNS) and experiments. (a) Mean axial vertical velocity versus $z$ against the DNS data for weak fountains by Lin and Armfield (2000). (b) Mean vertical velocity profiles in the cross-sections along the jet axis in the thermocline (curves) against the experimental data on turbulent jets in a stratified fluid by Ezhova and Troitskaya (2012) (symbols). . . . . 46
849		
850		
851		
852		
853	<b>Fig. 4.</b>	Illustration of the jet in a stratified fluid by surfaces of constant vertical velocity and temperature for the thick thermocline, $Fr = 22$ ( $Fr_t = 1.89$ ). Waves are visualized by surfaces of constant temperature $T = 0.03$ and $T = 0.97$ . . . . . 47
854		
855		
856	<b>Fig. 5.</b>	Magnitude of the mean flow velocity for $Fr=7$ ( $Fr_t = 0.6$ ) (a,d), 13 (1.11) (b,e), 22 (1.89) (c,f) (upper panel - thin thermocline, lower panel - thick thermocline). Dashed curves correspond to the contour lines of temperature $T = 0.1$ and $T = 0.9$ . . . . . 48
857		
858		
859	<b>Fig. 6.</b>	(a) Mean centerline velocities for the jet in a homogeneous fluid and for all the simulations in the stratified media indicating mean jet penetration. (b) Theoretical prediction of the mean penetration height versus the Froude number: $\gamma = 2$ (solid), $\gamma = 0.5$ (dashed). Symbols ■ and □ denote the mean heights obtained in the simulations for $\gamma = 2$ and $\gamma = 0.5$ respectively. . . . . 49
860		
861		
862		
863	<b>Fig. 7.</b>	The instantaneous temperature (left) and vertical velocity (right) fields in the thermocline for both stratifications. . . . . 50
864		
865	<b>Fig. 8.</b>	(a) Velocity profiles of the gravity currents propagating at the level of neutral buoyancy at a distance $r = 20$ from the jet axis (gray curves - thin thermocline, black curves - thick thermocline). (b) Average temperature of the gravity current as a function of the thermocline Froude number. (c) Entrainment flux obtained from (17) as a function of the thermocline Froude number. . . . . 51
866		
867		
868		
869		
870	<b>Fig. 9.</b>	Mean horizontal velocity fields in the jet impinging on the thermocline for $Fr = 16$ ( $Fr_t = 1.37$ ): (a) - thin thermocline, (b) - thick thermocline. . . . . 52
871		
872	<b>Fig. 10.</b>	Instantaneous temperature field in the horizontal plane at the center of the thermocline and time history of the isotherms at distance $r = 20$ from the jet center. The data in the upper panel pertain the simulation of the thin thermocline with $Fr = 10$ ( $Fr_t = 0.86$ ) (isotherms corresponding to temperatures from $T = 0.4$ to $T = 0.7$ ) and at the lower panel - the simulation with the $Fr = 22$ ( $Fr_t = 1.89$ ) (isotherms from $T = 0.3$ to $T = 0.7$ ). . . . . 53
873		
874		
875		
876		
877	<b>Fig. 11.</b>	(a) The spectra of jet oscillations in the thin (solid) and thick thermocline (dashed) for $Fr = 13$ ( $Fr_t = 1.11$ ). (b) The spectra of jet oscillations (dashed) and internal waves (solid), thin
878		

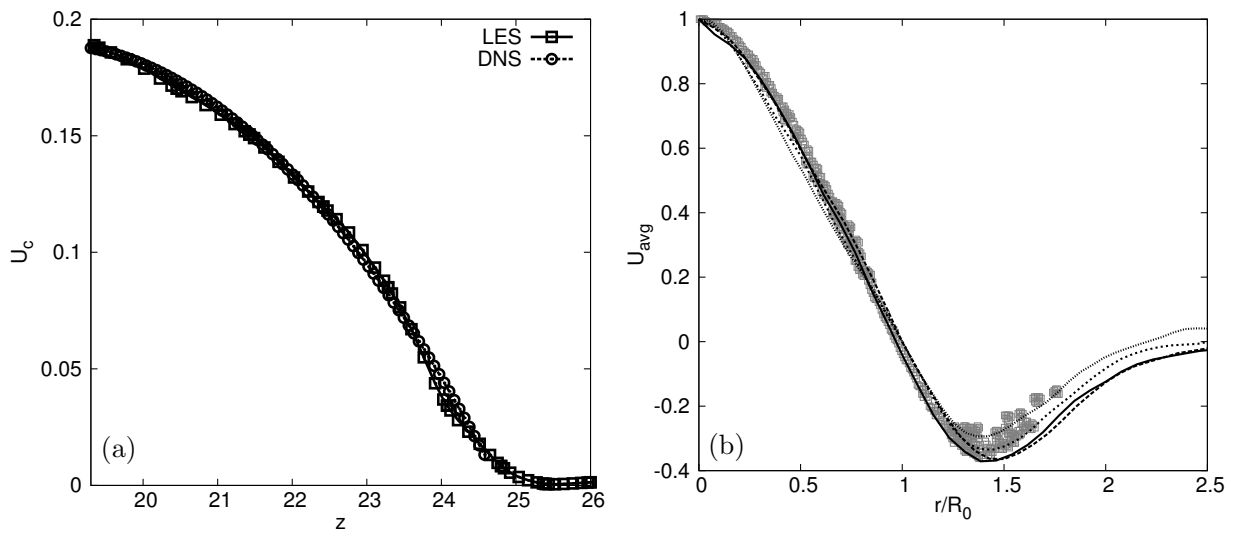
879	thermocline. (c) The spectra of jet oscillations (dashed) and internal waves (solid), thick	
880	thermocline. . . . .	54
881	<b>Fig. 12.</b> The frequencies of the jet oscillations and internal waves as the functions of the Froude	
882	number: (a) thin thermocline, (b) thick thermocline. The solid curves correspond to the	
883	maximal buoyancy frequency. . . . .	55
884	<b>Fig. 13.</b> (a) The amplitudes of the jet oscillations and the internal waves as function of the thermo-	
885	cline Froude number. Solid line represents the stationary solution of Landau equation. (b)	
886	The group velocity of the first mode of internal waves as a function of frequency. . . . .	56
887	<b>Fig. 14.</b> Vertical profiles of the energy flux of internal waves: upper panel - thin thermocline, lower	
888	panel - thick thermocline. Left: $r = 20$ , right: $r = 25$ . . . . .	57
889	<b>Fig. 15.</b> The surface-integrated wave energy flux normalized with the jet energy flux at the entrance	
890	to the thermocline. The values at the largest Froude number for the distance $r = 20$ coincide. . . . .	58
891	<b>Fig. A1.</b> The mesh and instantaneous temperature fields for $Fr = 13$ ( $Fr_t = 1.11$ ), thin thermocline,	
892	in (a) the regular simulations and (b) in the validation case. (c) Average centerline velocities	
893	for the test case and in regular simulations. Average velocity magnitude: (d) in the regular	
894	simulations and (e) in the test case. Dashed curves denote the contour lines of average	
895	temperature $T = 0.1$ and $T = 0.9$ . . . . .	59
896	<b>Fig. A2.</b> The examples of the isotherms $T = 0.5$ and average spectra at $r = 20$ and $r = 25$ for the thin	
897	thermocline (upper panel) and the thick thermocline (lower panel). . . . .	60



898 FIG. 1. Left panel: domain configuration for the turbulent jet in a homogeneous fluid. The jet is shown by the  
 899 contour surface of vertical velocity  $u_z = 0.03$ . Right panel: an inflow velocity profile.

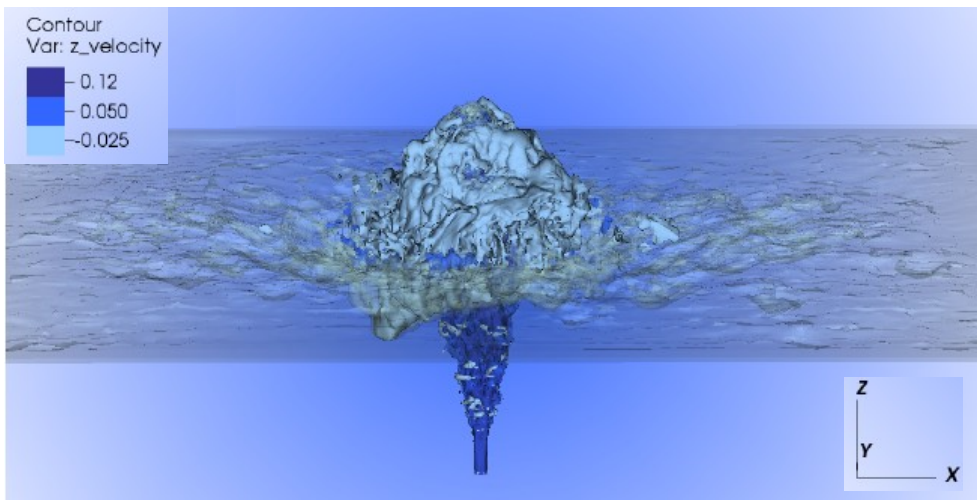


900 FIG. 2. (a) Inverse mean centerline velocity as a function of the distance from the nozzle (black dots - LES  
 901 data, gray - theory). (b) The far-field  $z$ -velocity profile, (c) turbulent stresses  $\langle u_z'^2 \rangle / U_c^2$  and (d)  $\langle u_r'^2 \rangle / U_c^2$ .  
 902 The data for comparison are available from the following papers: 'DNS round' - Picano and Casciola (2007),  
 903 'DNS annular' - Picano and Hanjalic (2012), 'exp Re=11 000' - Panchapakesan and Lumley (1993), 'exp Re=95  
 904 000' - Hussein et al. (1994).

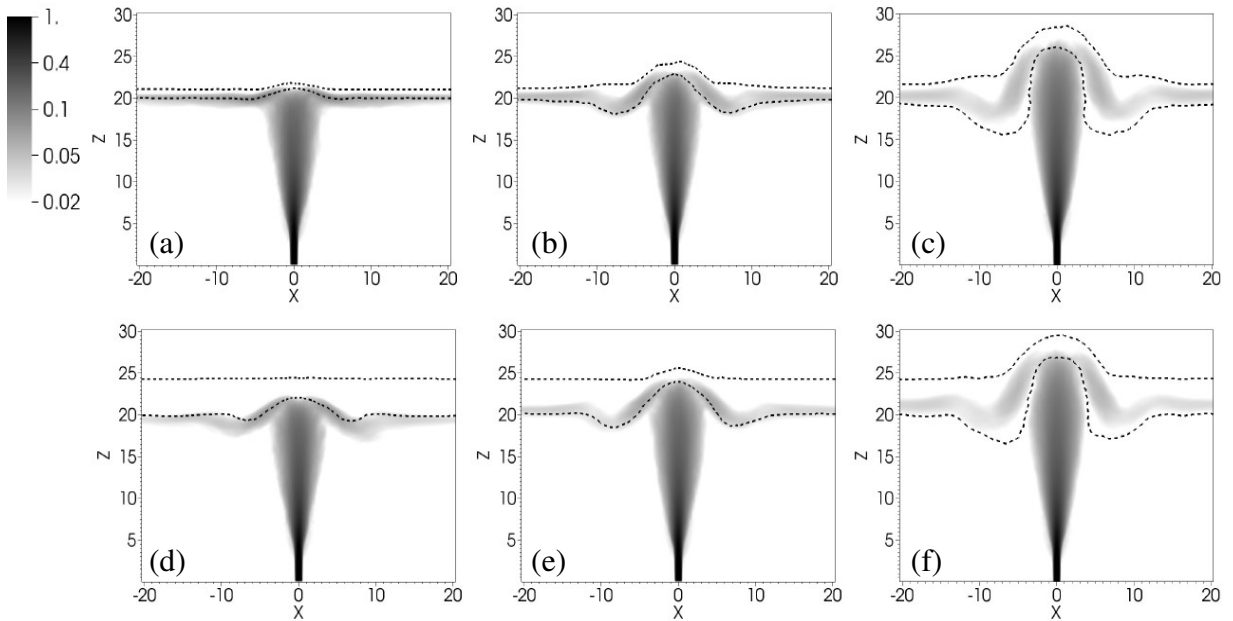


905 FIG. 3. Comparison of present LES data with direct numerical simulations (DNS) and experiments. (a)  
 906 Mean axial vertical velocity versus  $z$  against the DNS data for weak fountains by Lin and Armfield (2000). (b)  
 907 Mean vertical velocity profiles in the cross-sections along the jet axis in the thermocline (curves) against the  
 908 experimental data on turbulent jets in a stratified fluid by Ezhova and Troitskaya (2012) (symbols).

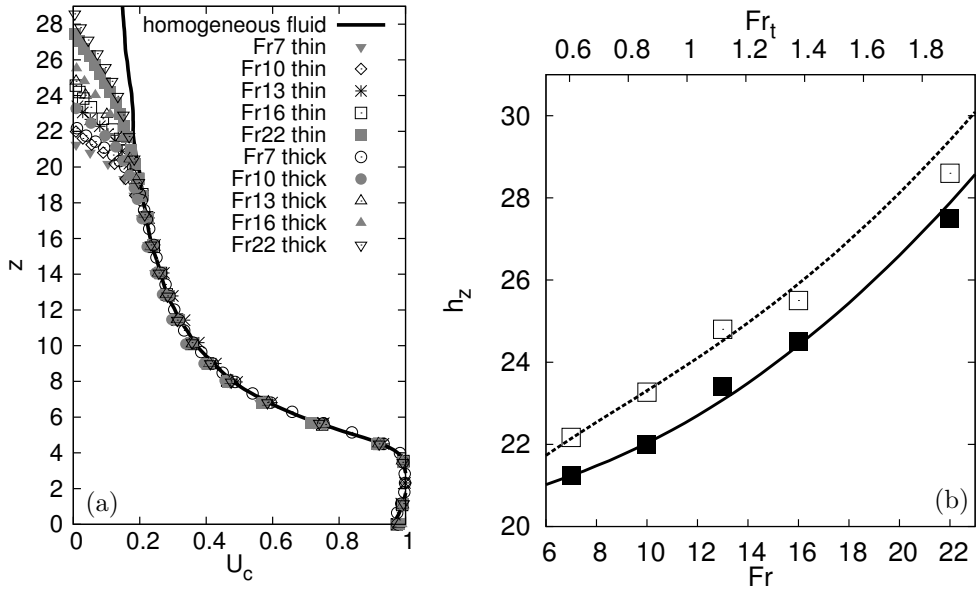




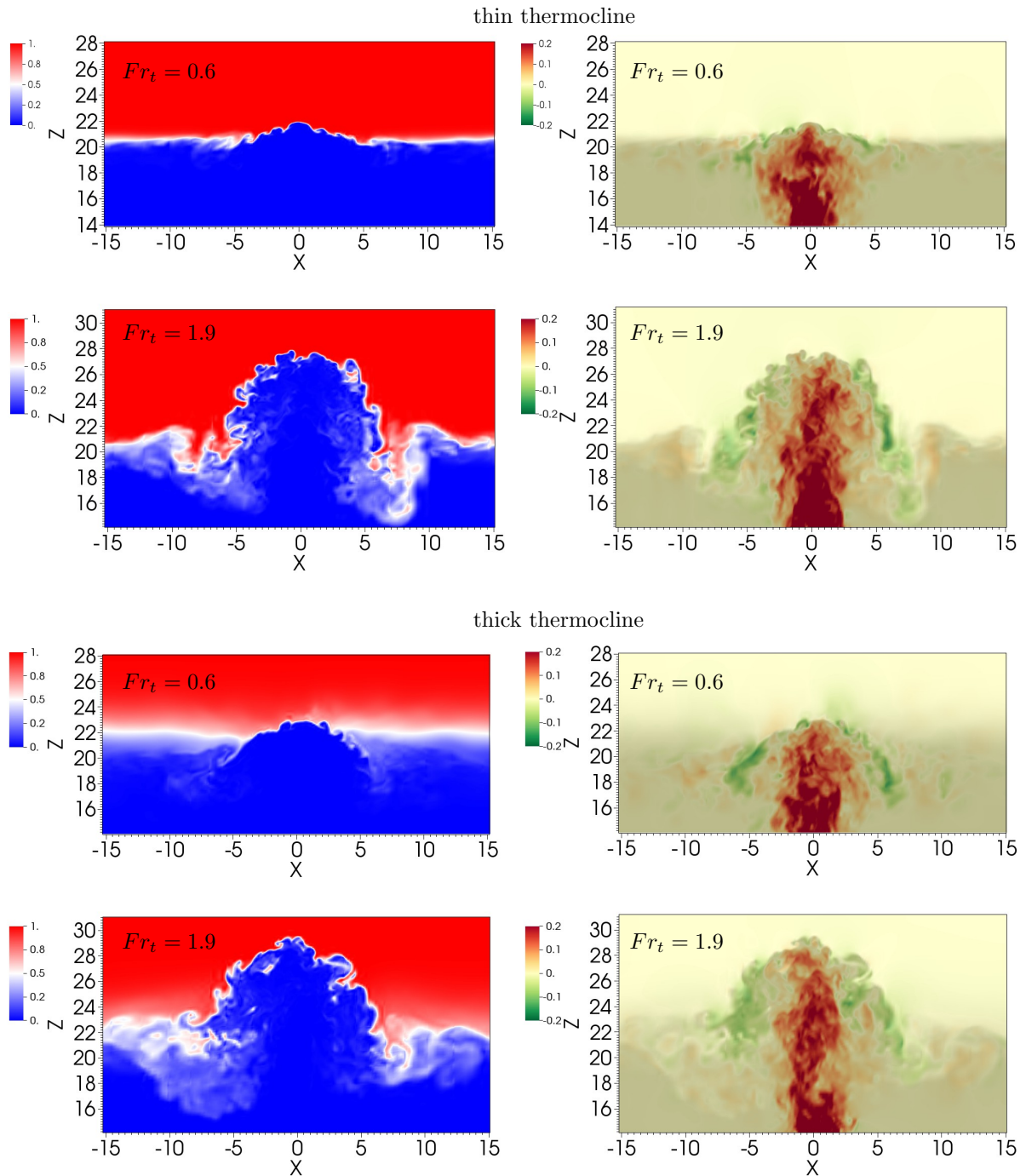
909 FIG. 4. Illustration of the jet in a stratified fluid by surfaces of constant vertical velocity and temperature for  
 910 the thick thermocline,  $Fr = 22$  ( $Fr_t = 1.89$ ). Waves are visualized by surfaces of constant temperature  $T = 0.03$   
 911 and  $T = 0.97$ .



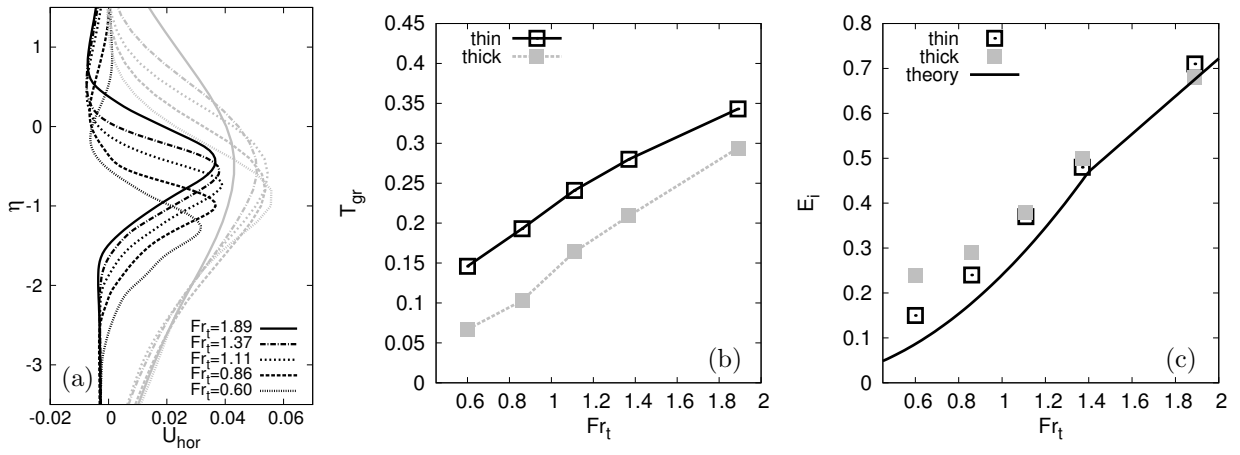
912 FIG. 5. Magnitude of the mean flow velocity for  $Fr=7$  ( $Fr_t = 0.6$ ) (a,d), 13 (1.11) (b,e), 22 (1.89) (c,f) (upper  
 913 panel - thin thermocline, lower panel - thick thermocline). Dashed curves correspond to the contour lines of  
 914 temperature  $T = 0.1$  and  $T = 0.9$ .



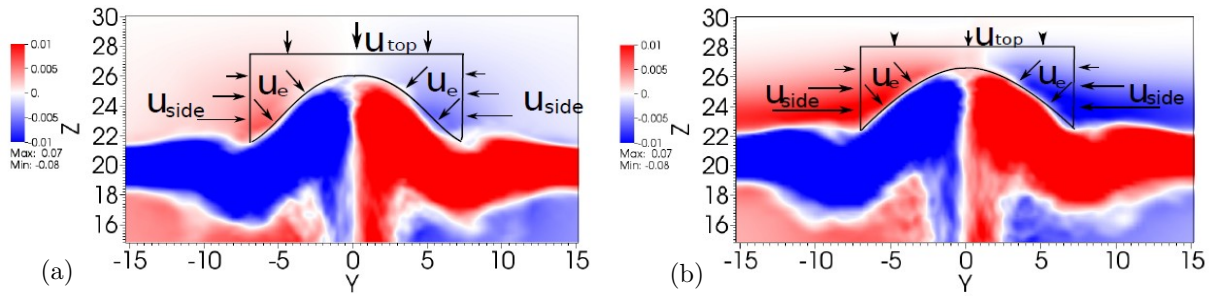
915 FIG. 6. (a) Mean centerline velocities for the jet in a homogeneous fluid and for all the simulations in the  
 916 stratified media indicating mean jet penetration. (b) Theoretical prediction of the mean penetration height versus  
 917 the Froude number:  $\gamma = 2$  (solid),  $\gamma = 0.5$  (dashed). Symbols  $\blacksquare$  and  $\square$  denote the mean heights obtained in the  
 918 simulations for  $\gamma = 2$  and  $\gamma = 0.5$  respectively.



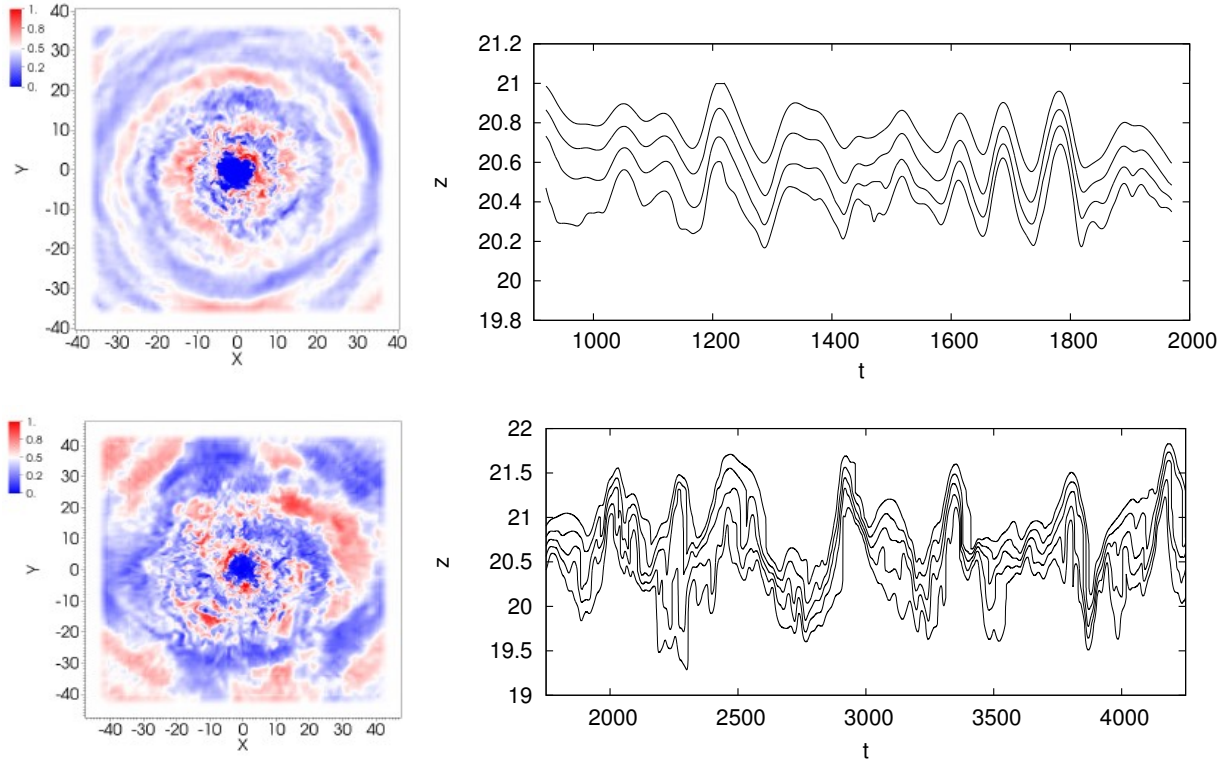
919 FIG. 7. The instantaneous temperature (left) and vertical velocity (right) fields in the thermocline for both  
 920 stratifications.



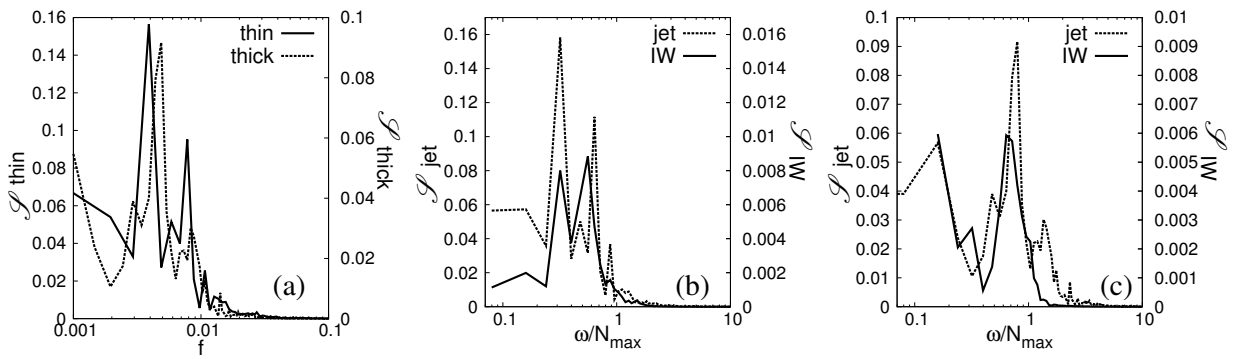
921 FIG. 8. (a) Velocity profiles of the gravity currents propagating at the level of neutral buoyancy at a distance  
 922  $r = 20$  from the jet axis (gray curves - thin thermocline, black curves - thick thermocline). (b) Average temper-  
 923 ature of the gravity current as a function of the thermocline Froude number. (c) Entrainment flux obtained from  
 924 (17) as a function of the thermocline Froude number.



925 FIG. 9. Mean horizontal velocity fields in the jet impinging on the thermocline for  $Fr = 16$  ( $Fr_t = 1.37$ ): (a)  
 926 - thin thermocline, (b) - thick thermocline.

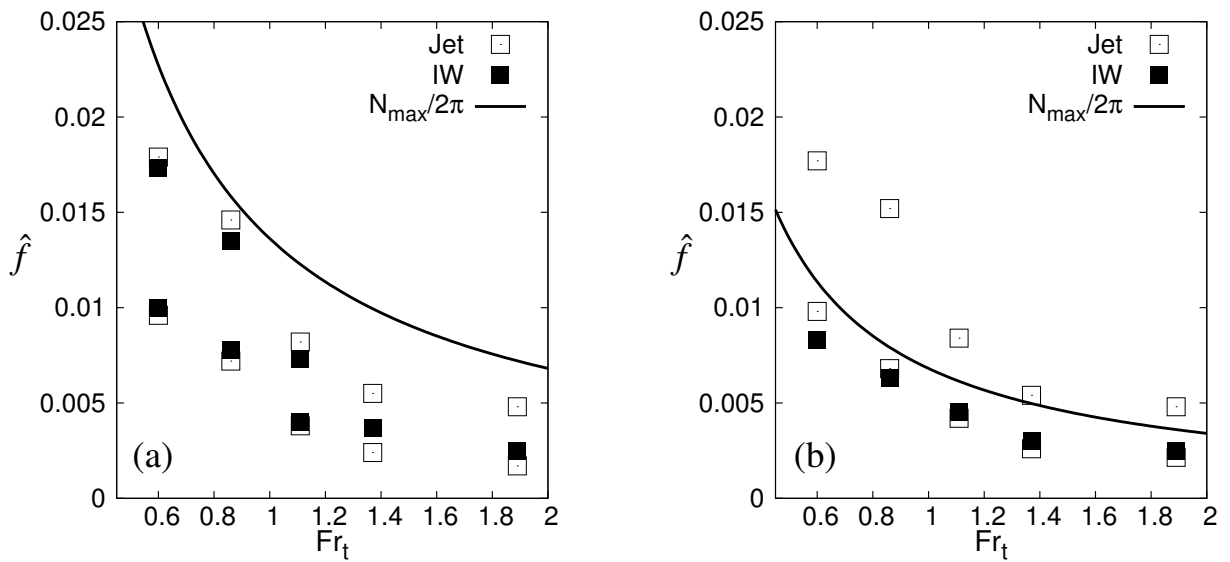


927 FIG. 10. Instantaneous temperature field in the horizontal plane at the center of the thermocline and time  
 928 history of the isotherms at distance  $r = 20$  from the jet center. The data in the upper panel pertain the simulation  
 929 of the thin thermocline with  $Fr = 10$  ( $Fr_t = 0.86$ ) (isotherms corresponding to temperatures from  $T = 0.4$  to  
 930  $T = 0.7$ ) and at the lower panel - the simulation with the  $Fr = 22$  ( $Fr_t = 1.89$ ) (isotherms from  $T = 0.3$  to  
 931  $T = 0.7$ ).

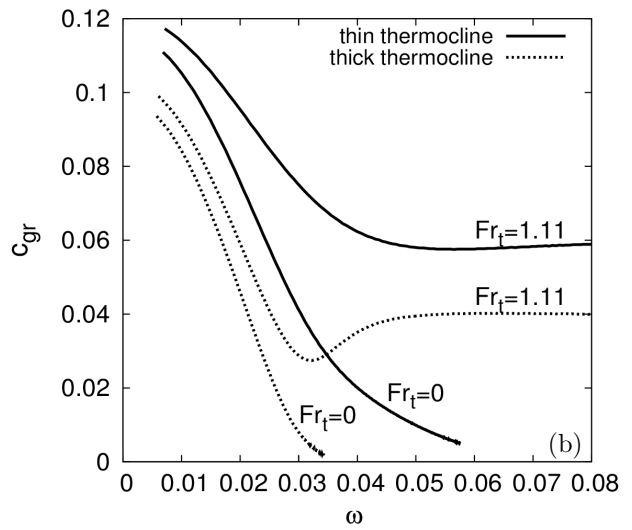
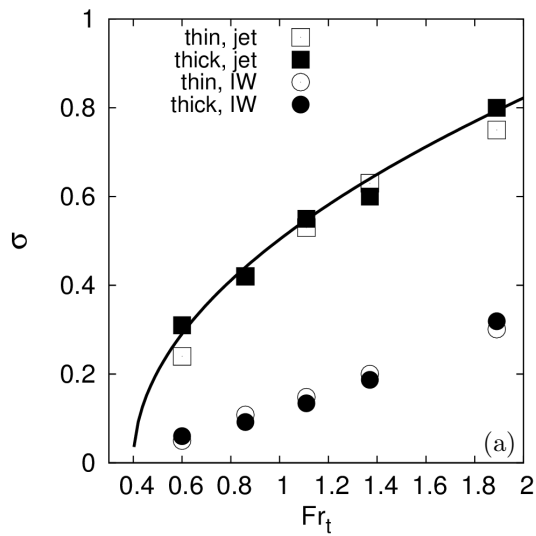


932 FIG. 11. (a) The spectra of jet oscillations in the thin (solid) and thick thermocline (dashed) for  $Fr = 13$   
 933 ( $Fr_t = 1.11$ ). (b) The spectra of jet oscillations (dashed) and internal waves (solid), thin thermocline. (c) The  
 934 spectra of jet oscillations (dashed) and internal waves (solid), thick thermocline.

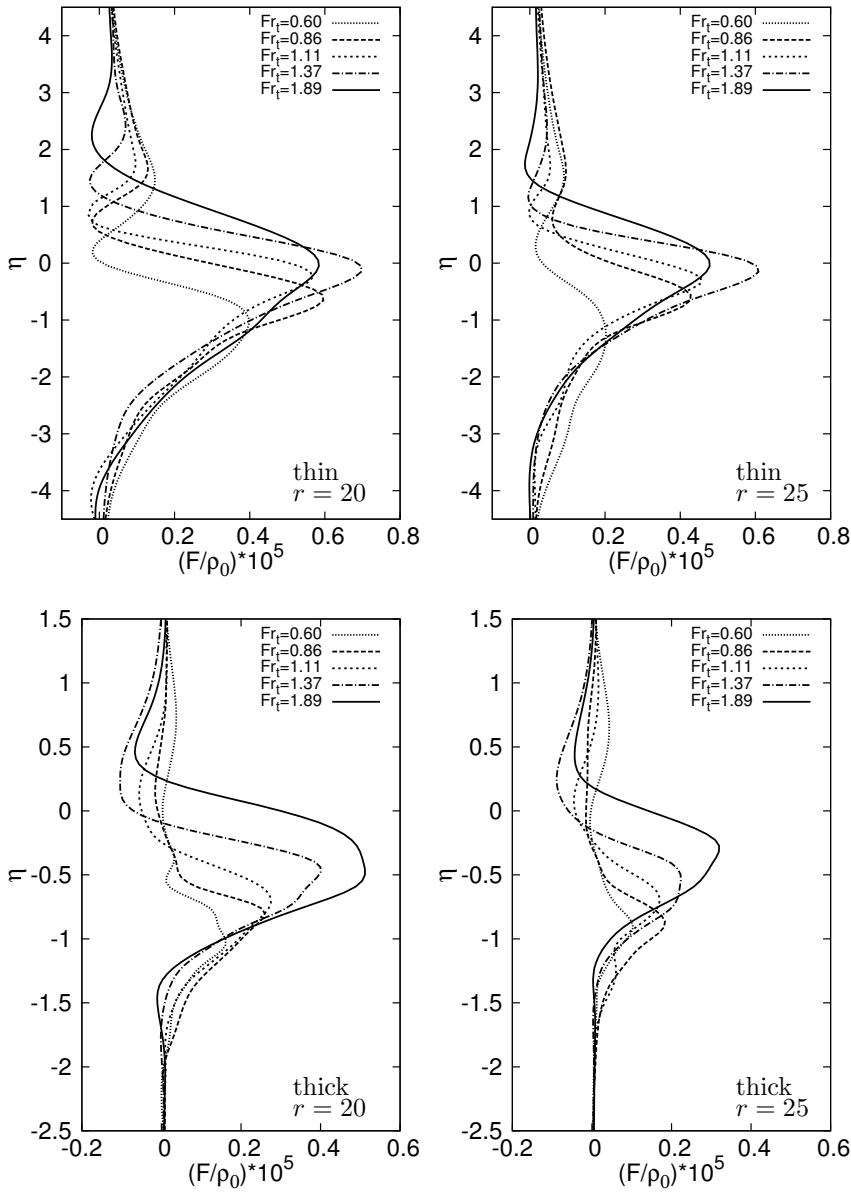




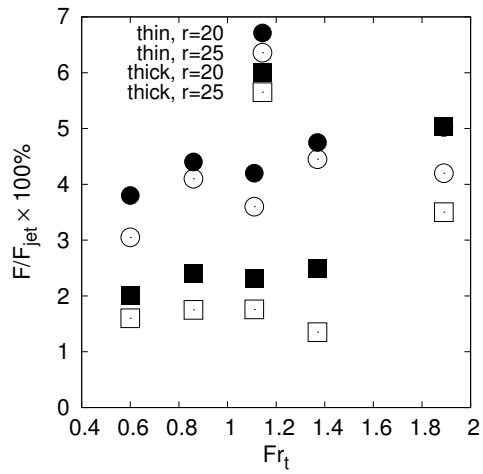
935 FIG. 12. The frequencies of the jet oscillations and internal waves as the functions of the Froude number: (a)  
 936 thin thermocline, (b) thick thermocline. The solid curves correspond to the maximal buoyancy frequency.



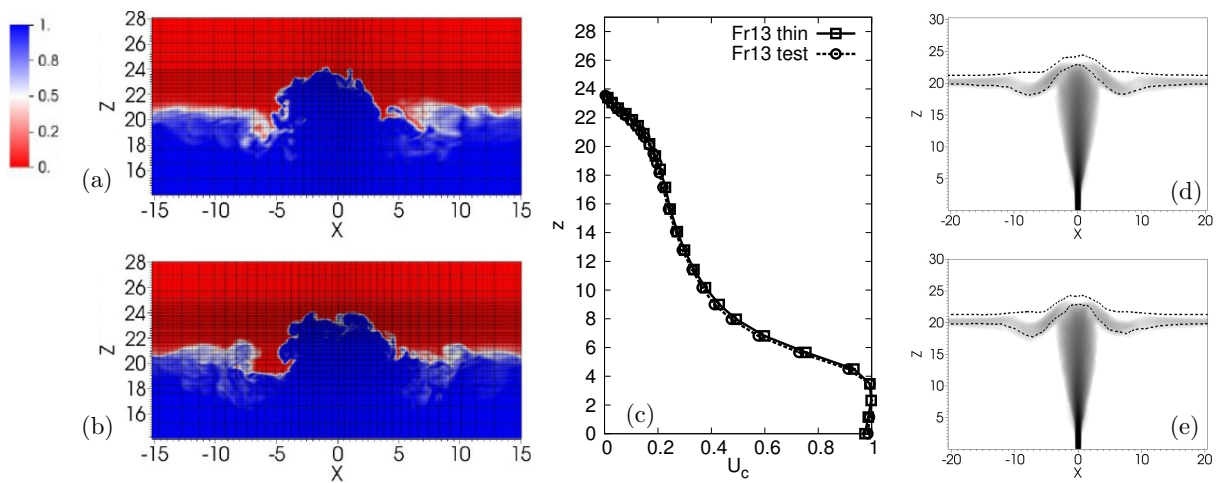
937 FIG. 13. (a) The amplitudes of the jet oscillations and the internal waves as function of the thermocline  
 938 Froude number. Solid line represents the stationary solution of Landau equation. (b) The group velocity of the  
 939 first mode of internal waves as a function of frequency.



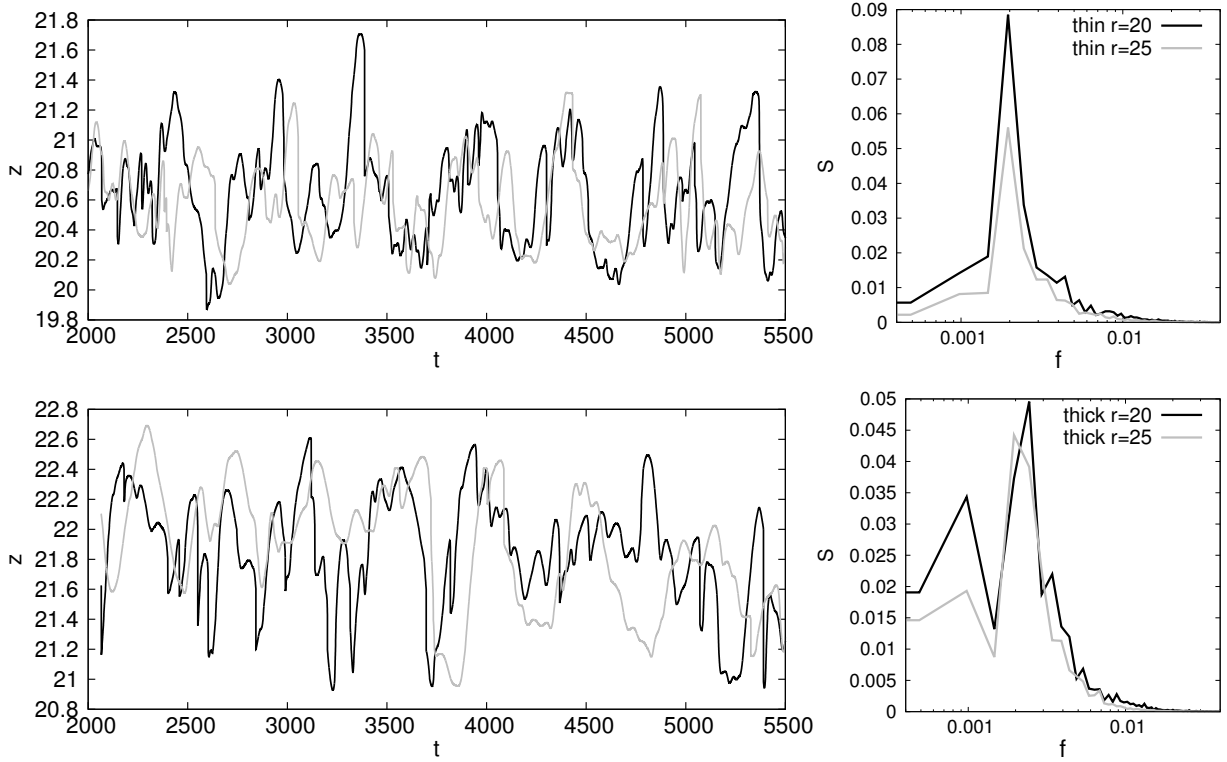
940 FIG. 14. Vertical profiles of the energy flux of internal waves: upper panel - thin thermocline, lower panel -  
 941 thick thermocline. Left:  $r = 20$ , right:  $r = 25$ .



942 FIG. 15. The surface-integrated wave energy flux normalized with the jet energy flux at the entrance to the  
 943 thermocline. The values at the largest Froude number for the distance  $r = 20$  coincide.



944 Fig. A1. The mesh and instantaneous temperature fields for  $Fr = 13 (Fr_t = 1.11)$ , thin thermocline, in (a)  
 945 the regular simulations and (b) in the validation case. (c) Average centerline velocities for the test case and in  
 946 regular simulations. Average velocity magnitude: (d) in the regular simulations and (e) in the test case. Dashed  
 947 curves denote the contour lines of average temperature  $T = 0.1$  and  $T = 0.9$ .



948 Fig. A2. The examples of the isotherms  $T = 0.5$  and average spectra at  $r = 20$  and  $r = 25$  for the thin  
 949 thermocline (upper panel) and the thick thermocline (lower panel).